

# Simulation of diffusive particle propagation and related $\gamma$ -ray emission from proton-proton interactions at the Galactic Center

## Masterarbeit aus der Physik

vorgelegt von

**Alexander Ziegler**

am 28.10.2014

Erlangen Centre for Astroparticle Physics  
Physikalisches Institut 1  
Lehrstuhl für Astroteilchenphysik  
Friedrich-Alexander-Universität  
Erlangen-Nürnberg



1. Gutachter: Prof. Dr. Christopher van Eldik
2. Gutachter: Prof. Dr. Jörn Wilms



## Abstract

A few years ago, an extended region of diffuse very-high-energy  $\gamma$ -ray emission was detected at the Galactic Center with the H.E.S.S. instrument. In the scope of this thesis a possible scenario explaining the origin of the observed radiation is analyzed. It is assumed that the TeV  $\gamma$ -rays arise from interactions of diffusing hadronic cosmic rays with the molecular matter present in the region. The highly energetic hadronic particles are assumed to have been accelerated by a single central source located at the Galactic Center. A supernova explosion about  $10^4$  years ago could have delivered the energy amount required for particle acceleration. This thesis presents a numerical approach to charged-particle motion in turbulent magnetic fields. The aim is a derivation of diffusion coefficients from a statistical analysis of ensemble particle tracking with regard to the environmental conditions in the Galactic Center region. Typical values obtained for the diffusion coefficient are  $D_{10} \sim 10^{25} \text{ cm}^2/\text{s}$ . The derived diffusion coefficients serve as input parameters for a simulation which was developed in the second part of this thesis to model the diffuse  $\gamma$ -ray emission from the Galactic Center region. The results of this modeling are presented and compared to the H.E.S.S. measurement. This comparison includes both the analysis of calculated  $\gamma$ -ray spectra and the morphology of the simulated emission. For diffusion coefficients of  $D_{10} \sim 10^{28} \text{ cm}^2/\text{s}$ , the results of the simulation can reproduce the characteristics of the observed emission generally quite well. In contrast to that, the observed emission cannot be reproduced when applying the diffusion coefficients  $D_{10} \sim 10^{25} \text{ cm}^2/\text{s}$ , which have been derived in this work.

## Kurzfassung

Im Galaktischen Zentrum wurde mit den H.E.S.S. Teleskopen vor wenigen Jahren ein ausgedehntes Band sehr hochenergetischer diffuser  $\gamma$ -Strahlung entdeckt. In dieser Masterarbeit wird ein mögliches Szenario, das den Ursprung dieser Strahlung erklären könnte, genauer untersucht. Es wird angenommen, dass die  $\gamma$ -Strahlung durch Wechselwirkungsprozesse zwischen hochenergetischen, diffundierenden hadronischen Teilchen und dem molekularen Material in der Region entsteht. Ferner geht man davon aus, dass die diffundierenden Teilchen in einer einzelnen Quelle im Galaktischen Zentrum, beispielsweise durch eine Supernova-Explosion vor  $10^4$  Jahren, beschleunigt wurden. In dieser Arbeit wird die Bewegung geladener Teilchen in turbulenten Magnetfeldern numerisch simuliert. Das Ziel dabei ist es, Diffusionskoeffizienten für eine Umgebung wie das Galaktische Zentrum aus der statistischen Analyse der Bewegung von Vielteilchensystemen abzuleiten. Die ermittelten Werte liegen in der Größenordnung von  $D_{10} \sim 10^{25} \text{ cm}^2/\text{s}$ . Diese Diffusionskoeffizienten werden als Parameter für die im zweiten Teil der Arbeit entwickelte Simulation benötigt, mit der die diffuse  $\gamma$ -Strahlung im Galaktischen Zentrum modelliert werden kann. Die Ergebnisse dieser Simulation werden präsentiert und mit denen der H.E.S.S. Analyse verglichen. Für diesen Vergleich wird neben den Energiespektren auch die Morphologie der simulierten Strahlung analysiert. Die erzielten Ergebnisse zeigen, dass die gemessenen Daten für Diffusionskoeffizienten in der Größenordnung von  $D_{10} \sim 10^{28} \text{ cm}^2/\text{s}$  im Allgemeinen gut durch die Ergebnisse der Simulation beschrieben werden können. Allerdings zeigt sich, dass für die im ersten Teil der Arbeit abgeleiteten Diffusionskoeffizienten, die in der Größenordnung von  $D_{10} \sim 10^{25} \text{ cm}^2/\text{s}$  liegen, die Charakteristiken der gemessenen Strahlung nicht reproduziert werden können.



# Contents

<b>1</b>	<b>Introduction</b>	<b>1</b>
<b>2</b>	<b>Diffuse <math>\gamma</math>-ray emission from the Galactic Center region</b>	<b>3</b>
2.1	Observation with the H.E.S.S. instrument . . . . .	3
2.2	The hadronic diffusion scenario as origin of the diffuse $\gamma$ -ray emission . . . . .	5
<b>3</b>	<b>A numerical approach to charged-particle motion in turbulent magnetic fields</b>	<b>8</b>
3.1	Physical background . . . . .	8
3.1.1	Field particle interaction . . . . .	8
3.1.2	Diffusion of cosmic rays . . . . .	10
3.2	Simulating particle propagation by ensemble tracking . . . . .	12
3.2.1	Modeling of the turbulent magnetic field . . . . .	12
3.2.2	Single particle tracking . . . . .	13
3.2.3	Ensemble tracking and output measures . . . . .	14
3.2.4	Influence of model parameters . . . . .	17
3.3	Application to the Galactic Center region . . . . .	20
3.3.1	Environmental conditions and parameter settings . . . . .	21
3.3.2	Extraction of diffusion coefficients . . . . .	22
<b>4</b>	<b>Modeling the diffuse <math>\gamma</math>-ray emission from the Galactic Center region</b>	<b>29</b>
4.1	The model . . . . .	29
4.1.1	Long-distance particle tracking . . . . .	29
4.1.2	Density map of molecular clouds . . . . .	31
4.1.3	Simulation procedure and interaction processes . . . . .	33
4.2	Results of the modeling and comparison to the H.E.S.S. data . . . . .	35
4.2.1	Results for commonly proposed diffusion coefficients . . . . .	35
4.2.2	Results for diffusion coefficients derived in this work . . . . .	44
<b>5</b>	<b>Conclusion and outlook</b>	<b>51</b>
	<b>Appendix</b>	<b>55</b>
	<b>Bibliography</b>	<b>57</b>



# 1 Introduction

The most powerful electromagnetic radiation in our universe is referred to as  $\gamma$ -radiation. Its photon energies range from about 100 keV up to the very-high-energy regime starting at approximately 100 GeV. In contrast to charged cosmic-ray particles, neutral  $\gamma$ -rays are not deflected by galactic magnetic fields during propagation through the Galaxy and thus point directly back to their point of origin when being observed on earth.  $\gamma$ -rays predominantly arise from interactions of accelerated charged particles with ambient matter or electromagnetic radiation fields, the only exception being their production in top-down processes like the decay of heavy particles (Hinton & Hofmann 2009). Therefore, the study of  $\gamma$ -rays constitutes a compelling opportunity for developing a deeper understanding of astroparticle physics and related questions such as the origin and acceleration mechanisms of cosmic rays.

Very-high-energy (VHE)  $\gamma$ -rays are detected with ground-based Imaging Atmospheric-Cherenkov Telescopes (IACTs), which have the advantage of a very large collection area ( $\sim 10^5 \text{ m}^2$ ) when being compared to satellite-based instruments. Since the detection of the first TeV  $\gamma$ -ray source in 1989, the Crab Nebula (Weekes et al. 1989), the following discovery of so far  $\sim 150$  sources of very-high-energy has helped to establish this relatively young field of astronomy. Detected sources comprise extragalactic sources at high latitudes, identified as active galactic nuclei, and a distribution of Galactic TeV emitters located along the Galactic equator. Galactic sources include shell type supernova remnants, where emission is probably attributed to high-energy protons accelerated in their shells, pulsar wind nebulae, binary systems and the Galactic Center (Hinton & Hofmann 2009; TeVCat 2014).

A large contribution to these discoveries was made by observations conducted with the High Energy Stereoscopic System (H.E.S.S.), which provides an optimal view on the Galactic Center region due to its location in the Khomas Highland of Namibia in the southern hemisphere. Representing the nearest galactic nucleus, the Galactic Center region includes the supermassive black hole Sagittarius A\* (Sgr A\*) at its center, surrounded by massive clouds of dense molecular material. This combination provides a unique possibility of studying non-thermal processes in our direct proximity, making the Galactic Center region object of dedicated observations with the H.E.S.S. instrument. In addition to the detection of a very bright point source spatially located at the center of our Galaxy, an extended region of so-called diffuse  $\gamma$ -ray emission was observed (Aharonian et al. 2006a). The origin of this diffuse emission is subject of current research. A possible scenario assumes that relativistic hadrons, accelerated by a central source, are deflected by turbulent magnetic fields and diffuse away from their point of origin, producing the observable emission through interactions with ambient matter.

The aim of this work is to assess the validity of the hadronic diffusion scenario as origin of the diffuse very-high-energy  $\gamma$ -ray emission observed at the Galactic Center by simulating charged-particle motion in turbulent magnetic fields and modeling the  $\gamma$ -ray emission resulting from the interactions of diffusing particles with ambient matter. This work is

organized as follows:

In Chapter 2, the experimental discovery of the diffuse  $\gamma$ -ray emission made with the H.E.S.S. experiment is presented alongside the suggested diffusion hypothesis. In Chapter 3, a numerical treatment of charged-particle motion in turbulent magnetic fields is introduced. In this context, diffusion coefficients are derived with regard to the physical conditions of the Galactic Center region. In Chapter 4, a simulation to model the diffuse  $\gamma$ -ray emission from the Galactic Center region is presented. In the developed formalism, the diffusion coefficient enters as a free input parameter. The simulation is performed using commonly suggested diffusion coefficients as well as those derived in this work. Finally, in Chapter 5, the results obtained in this thesis are summarized and a brief outlook is given.

## 2 Diffuse $\gamma$ -ray emission from the Galactic Center region

Observations of the Galactic Center region with satellite-based  $\gamma$ -ray detectors like EGRET, which work in the sub-TeV range, already reported the detection of a source near the spatial position of Sgr A\* in 1998 (Mayer-Hasselwander et al. 1998). Although a hadronic origin by enhanced cosmic rays is discussed for the observed high-energy emission, this interpretation remains highly speculative besides several other proposed scenarios, including a production via inverse Compton scattering (see Mayer-Hasselwander et al. 1998). So far, the production mechanism of this high-energy  $\gamma$ -radiation has remained unknown. Observations of the Galactic Center region in the TeV range, made with the H.E.S.S. instrument, led to the detection of an extended region of so-called diffuse very-high-energy  $\gamma$ -ray emission, in addition to the detection of two outstanding point sources. The experimental measurement, presented by Aharonian et al. (2006a), is discussed in the subsequent section. The large spatial extension of the diffuse signal makes a production via inverse Compton scattering of high-energy electrons rather unlikely. Moreover, the spatial correlation between the observed excess and the density distribution of molecular gas hints towards a hadronic diffusion scenario, which is discussed in the second part of this chapter.

### 2.1 Observation with the H.E.S.S. instrument

Observations of the Galactic Center region with the H.E.S.S. instrument revealed a strong point source at the gravitational center of our Galaxy in 2004, namely HESS J1745-290 (Aharonian et al. 2004). At that time, the spatial position of this source was compatible with the supermassive black hole Sgr A\*, the supernova remnant Sgr A East and a Galactic Center point source detected by the Whipple (Kosack et al. 2004) and the Cangaroo II (Tsuchiya et al. 2004) experiments. Further analysis of that region with the H.E.S.S. instrument led to the detection of a second point source, the supernova remnant/pulsar wind nebula G0.9+0.1 (Aharonian et al. 2005a). These two point sources are clearly visible in Fig. 2.1a. Due to the improved angular resolution, which is better than  $0.1^\circ$ , and the greater sensitivity of the H.E.S.S. instrument compared to previous VHE instruments, it is possible to subtract the two point sources at the observed positions. This procedure offers the possibility to search for much fainter emission masked by the bright point sources. For the analysis, 55 hours of data consisting of observations of Sgr A\* and G0.9+0.1, as well as a part of the data of the H.E.S.S. Galactic plane survey (Aharonian et al. 2005b) were used. The resulting  $\gamma$ -ray sky map is shown in Fig. 2.1b.

Two interesting regions of extended emission remain. The first one, HESS J1745-303, is located in the bottom right corner and is spatially coincident with the unidentified EGRET source 3EG J1744-3011 (Hartman et al. 1999). The mechanisms leading to this VHE emission are not yet fully understood as no appropriate counterpart at other wavelengths is observed (see Aharonian et al. (2008) for a discussion of possible scenarios). This subject

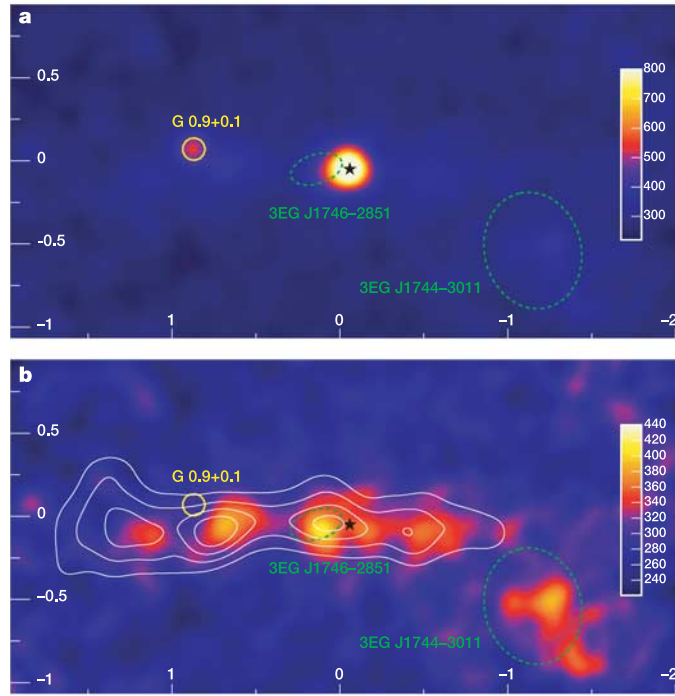


**Fig. 2.1:** **a**, VHE  $\gamma$ -ray count map of the Galactic Center region. **b**, same count map after subtraction of the two dominant point sources HESS J1745-290 and G0.9+0.1. Axes are Galactic longitude ( $x$ ) and Galactic latitude ( $y$ ). The color scale is dimensionless and corresponds to events detected within 55 hours of dedicated observation of the Galactic Center region. The position of Sgr A\* is labeled with a black star, the position and spatial extension of the supernova remnant G0.9+0.1 is indicated by a yellow circle. Dashed green ellipses mark the 95% confidence regions of the two unidentified EGRET sources. White contour lines depict the density of molecular gas (traced by its CS emission).

The excess spatially extended along the Galactic plane counts  $\sim 3500$   $\gamma$ -ray photons, the statistical significance is given as 14.6 standard deviations. To improve signal/noise and angular resolution, tight selection cuts are applied with an energy threshold of 380 GeV (picture taken from Aharonian et al. 2006a).

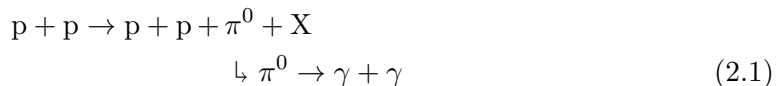
is not part of further discussion in this work.

The second one extends over a wide range in Galactic longitude ( $\sim 2^\circ$ ), and is also clearly visible in Galactic latitude ( $\sim 0.5^\circ$ ). The emission arising from this region is referred to as diffuse  $\gamma$ -ray emission. A possible scenario for the production of this emission and hints leading to this assumption are presented in the following section.

For completeness, it should be noted that new analysis of the central source HESS J1745-209 enabled a more precise measurement of its spectral properties (Aharonian et al. 2009) as well as an improved position determination (The HESS Collaboration: Acero et al. 2009). This led to the exclusion of Sgr A East as the dominant source of the emission of HESS J1745-209 with high probability. Additionally, the energetic pulsar wind nebula G359.95-0.04, which was discovered near the Galactic Center by Chandra in 2006 (Wang et al. 2006), came up as a new candidate for HESS J1745-209 besides Sgr A\*.

## 2.2 The hadronic diffusion scenario as origin of the diffuse $\gamma$ -ray emission

One of the currently most promising scenarios, which could explain the origin of the described diffuse  $\gamma$ -ray excess, assumes that charged hadrons are accelerated in a point-like source at the Galactic Center and stream away from their power source after having finished the acceleration process. On their way outwards, these highly energetic charged particles are deflected by turbulent magnetic fields present in the Galactic Center region. Statistically, the movement of the particles as a whole can be described as a diffusion process (see Section 3.1). The observable  $\gamma$ -rays arise from the interactions of the diffusing particles with the ambient matter - molecular gas concentrated in dense clouds. In this work, protons will be used as representatives for the diffusing hadronic particles since protons are the predominant component of the known cosmic rays observable on earth. Even though molecular gas does not consist of pure molecular hydrogen, it is the very dominating component. In a very good approximation, different elements can be neglected for a description of the interaction processes (heavy elements are contained at a level of  $\sim 10^{-4}$  atoms per H nucleon in molecular gas, see e.g. Bolatto et al. 2013). Thus, interactions leading to  $\gamma$ -ray emission can be modeled as proton-proton interactions. In these interactions, primarily pions are produced, whereby neutral pions subsequently decay to  $\gamma$ -rays. A possible reaction is



where by the scattering of two protons  $p$  a neutral pion  $\pi^0$  is produced.  $X$  stands for additional particles which might be produced in this reaction, depending on the energies of the primary particles.

A good argument for the diffusion assumption is given by the observed spatial correlation between the density distribution of molecular clouds and the intensity of the observed  $\gamma$ -ray excess. This feature is clearly visible in Fig. 2.1b, where white contour lines illustrate the density distribution of molecular clouds, traced by line emission of CO and CS molecules (Oka et al. 1998; Tsuboi et al. 1999). Potential background signals in this area arising from the galactic cosmic-ray sea can be excluded regarding the measured energy spectrum. The measured flux in the central area (Galactic longitude  $|l| < 0.8^\circ$ , Galactic latitude  $|b| < 0.3^\circ$ ) is about a factor of 3–9 higher for energies above 1 TeV than the galactic cosmic-ray sea could produce (Aharonian et al. 2006a). In addition, the fact that the observed excess decreases at  $|l| \approx 1^\circ$  supports the diffusion scenario, as the diffusing particles simply have not traversed a larger distance yet, and is furthermore contradictory to a signal produced by a spatially constant particle population. A further striking argument is given by the fact that the spectrum can be modeled by a power law, resulting in a spectral index of  $\Gamma = 2.29 \pm 0.07_{\text{stat}} \pm 0.10_{\text{sys}}$ . This value is very similar to the one derived for the central source HESS J1745-290,  $\Gamma = 2.25 \pm 0.04_{\text{stat}} \pm 0.10_{\text{sys}}$ , being fitted by a pure power law (Aharonian et al. 2006b), and thereby associates the diffuse emission with the central source as possible power source for the acceleration processes. The energy required to accelerate charged hadronic particles producing a  $\gamma$ -ray excess as observed, is estimated to be  $\sim 10^{50}$  erg for an energy range of  $10^9$ – $10^{15}$  eV according to Aharonian et al. (2006a). This means that the required energy could have been delivered by a single supernova explosion, if only about 10% of the typical explosion energy of  $10^{51}$  erg was converted into acceleration processes. Therefore, the supernova remnant Sgr A East with an estimated

age of about  $10^4$  years (Maeda et al. 2002) provides a likely candidate for the central particle accelerator, besides the supermassive black hole Sgr A\* itself.

An alternative leptonic scenario for the origin of the diffuse emission is that a distribution of electron accelerators is located at the region of interest. Then, the radiation would be produced by highly energetic electrons via inverse Compton scattering. However, this scenario seems rather unlikely, since electrons would lose their energy very rapidly in an environment like the Galactic Center region (see Section 3.3.1) and one would expect to see a more point-like emission from several sources with the H.E.S.S. instrument. Moreover, such signals are also expected to be bright in the X-ray regime, and no such population has been detected so far.

Other proposed hadronic scenarios which could explain the observation of the described diffuse  $\gamma$ -ray emission include stochastic cosmic-ray acceleration by magnetic turbulence in the Galactic Center region (Fatuzzo & Melia 2012, 2014) and the scenario of a Galactic wind outflow. In the latter, a powerful wind advects previously accelerated particles out of the central region of the Galactic Center, and particle transport would become energy independent (see e.g. Crocker et al. 2011).

### **Current status**

While working with the diffusion scenario, it is crucial to understand the motion of charged particles in turbulent magnetic fields. The central quantity for a statistical description is given by the **diffusion coefficient  $D$** , which statistically describes the movement of protons on their way out of the Galactic Center. In (Aharonian et al. 2006a), an upper limit estimate on the diffusion coefficient is given with a value of  $D \leq 10^{30} \text{ cm}^2/\text{s}$  ( $3.5 \text{ kpc}^2/\text{Myr}$ ). Here, the assumed source age of  $10^4$  years refers to Sgr A East as a possible source candidate and the limit is derived with a simple diffusion model, in which a possible energy dependence of the diffusion coefficient is neglected. Considering Sgr A\* itself a possible source, also source ages of about  $10^5$  years are suggested as the supermassive black hole might have had periods of stronger activity in the past. For the model applied by Aharonian et al. (2006a), this would simply mean that the diffusion coefficient scales down by the same factor as time scales up.

A couple of other authors working with different methods addressed the diffusion scenario in the center of our Galaxy after the experimental discovery of the diffuse emission by the H.E.S.S. experiment in 2006. Büsching et al. (2007) worked with an analytical method based on a simplification of the cosmic ray transport equation for protons with a mean energy of 3 TeV. For an impulsive injection of particles in a single supernova event they found a diffusion coefficient of  $D = 1 - 2 \text{ kpc}^2/\text{Myr}$ , in good agreement with the limit estimation given by Aharonian et al. (2006a). Another approach was used by Dimitrakoudis et al. (2009) in which particles are tracked in a density grid of molecular clouds. An energy dependence of  $D$  is taken into account and energy losses of protons during propagation are considered. Two main channels for possible proton-proton reactions were implemented in their simulation, and they obtained an optimal diffusion coefficient of  $D = 3.0 \pm 0.2 \text{ kpc}^2/\text{Myr}$  ( $E = 12.5 \text{ TeV}$ ), which is again in agreement with the H.E.S.S. limit. A parameter scan, not only of the diffusion coefficient  $D$  but also of its energy dependence  $D(E)$  and of the spectral index of the input proton spectrum, was carried out by Nekrasov (2010). Here, a three-dimensional density map for the distribution of molecular clouds was set up by using the results of an analysis of CO emission and OH absorption lines provided in (Sawada et al. 2004) to achieve a positioning of the molecular material along the line of sight. The results provided in (Kelner et al. 2006) were applied for a calculation of the

$\gamma$ -ray spectrum due to proton-proton interactions. The proton distribution is calculated by solving the diffusion equation in energy bins, while influences on the proton population during propagation are not taken into account. The results of the scan are in large part in agreement with the results of previous work. For a detailed discussion see Nekrassov (2010). Up to here, all named authors treated the problem by assuming the validity of the diffusion hypothesis, meaning that they determined the best parameters for the diffusion scenario by matching the output of their models to the measured data. In contrast, a different approach was made by Wommer et al. (2008). Determining the distribution of charged particles by tracking them in a turbulent magnetic field under exposure to the Lorentz force, these authors found that particles diffuse away from a central source too slowly to be able to produce the observed excess seen by H.E.S.S. This means that diffusion coefficients derived with this method should differ significantly from those derived by the authors mentioned before. Thus, there is some kind of disagreement between the results of the two different approaches.

In this work, a consistent treatment of the problem is pursued. In the following chapter, diffusion coefficients as a function of energy are extracted from an analysis of charged-particle motion in turbulent magnetic fields. Particles are treated as test particles and a typical value assumed for the magnetic field strength is  $50 \mu\text{G}$ . The applied methods are similar to those applied by Wommer et al. (2008). The derived parameters are used to simulate the diffusion of charged particles in the center of our Galaxy and the resulting  $\gamma$ -ray emission. The simulation works in different energy bins on a discrete three-dimensional space by a discretization of the diffusion equation. To set up a preferably realistic environment, the three dimensional cloud distribution constructed in (Nekrassov 2010) is used. Moreover, losses of protons due to interaction processes during propagation are taken into account. For the calculation of resulting  $\gamma$ -ray fluxes, the results presented by Kelner et al. (2006), giving a parametrization of the spectra of secondary particles produced at proton-proton collisions, are applied.

# 3 A numerical approach to charged-particle motion in turbulent magnetic fields

In this chapter, a numerical treatment of the motion of charged particles in turbulent magnetic fields is presented. In the first section, the physical background is introduced before turning to a numerical description in general. The method introduced by Giacalone & Jokipii (1994) is thereby used to generate a turbulent magnetic field. In the last section of this chapter, the established formalism is, under certain assumptions, applied to the physical conditions of the Galactic Center region. Here, the aim is a derivation of diffusion coefficients, which serve as input parameters for long-distance particle tracking (see Chapter 4).

## 3.1 Physical background

For the introduction of a numerical treatment of charged-particle motion in turbulent magnetic fields, it is necessary to first introduce the related physical background. Important physical quantities describing the dynamics of charged particles in magnetic fields are defined, and the field particle interaction topic is discussed. In a second step, a statistical description of the motion of charged particles in turbulent magnetic fields is given by the introduction of the diffusion equation.

### 3.1.1 Field particle interaction

The dynamics of a charged particle in a magnetic field  $\mathbf{B}$  are determined by the solution of the equation of motion

$$\frac{d}{dt} \mathbf{p} = q (\mathbf{v} \times \mathbf{B}) , \quad (3.1)$$

with the momentum  $\mathbf{p}$ , the velocity  $\mathbf{v}$  and the charge  $q$  of the considered particle. The time is denoted by  $t$ . The right hand side of this equation is referred to as Lorentz force, which acts on charged particles moving in a magnetic field. The easiest case is that of a homogeneous, static magnetic field, for which the solution of Eq. 3.1 is well-known. In the direction parallel to the uniform magnetic field, there is no influence on the initial movement and the particle moves straight on with a constant velocity  $\mathbf{v}_{\parallel}$ . In the direction perpendicular to  $\mathbf{B}$ , the particle moves in a circle with a constant velocity  $|\mathbf{v}_{\perp}|$ , due to a constant acceleration perpendicular to the plane containing both the velocity vector  $\mathbf{v}_{\perp}$  and the direction of the magnetic field. The described trajectory is illustrated in Fig. 3.1. Assuming for convenience  $\mathbf{B} = B \mathbf{e}_z$ , the solution in analytical form reads

$$\begin{aligned} x &= x_0 + r \sin(\omega t + \alpha) , \\ y &= y_0 + r \cos(\omega t + \alpha) , \\ z &= z_0 + v_z t . \end{aligned} \quad (3.2)$$

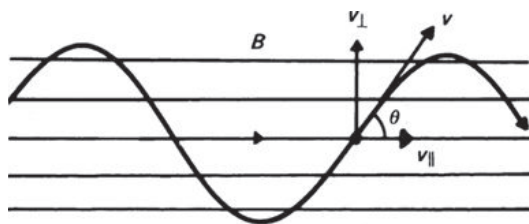


**Fig. 3.1:** Illustration of a particle trajectory in a homogeneous, static magnetic field. The circular movement takes place in the plane perpendicular to  $\mathbf{B}$  and  $\mathbf{v}_\perp$  and is therefore only indirectly visible in the shown projection. The picture is taken from Longair (2011).

The phase  $\alpha$  and the position  $(x_0, y_0, z_0)$  are set through the proper initial conditions. Within Eq. 3.2, two important quantities are introduced: first the *gyroradius* or *cyclotron radius* of the particle,

$$r = \frac{\gamma m |\mathbf{v}| \sin \theta}{q |\mathbf{B}|} , \quad (3.3)$$

where  $m$  denotes the rest mass of the particle and  $\gamma = 1/(1 - v^2/c^2)^{1/2}$ ,  $c$  being the speed of light.  $\theta$  is the so-called pitch angle, defined by  $\tan \theta = v_\perp/v_\parallel$ , i.e. the angle between  $\mathbf{v}$  and  $\mathbf{B}$ . The second important quantity is the *angular cyclotron frequency* or *angular gyrofrequency*

$$w = \frac{|\mathbf{v}_\perp|}{r} = \frac{q |\mathbf{B}|}{\gamma m} , \quad (3.4)$$

which is indirectly proportional to the time the particle needs for one gyration. For a more detailed discussion see e.g. Longair (2011).

The quantities defined above characterize the dynamics of charged particles in magnetic fields. In the following, the focus lies on turbulent magnetic fields and the dynamics of charged particles therein.

### Scattering of particles off turbulent magnetic fields

Irregularities in magnetic fields lead to scatterings of charged particles in pitch angle off the magnetic field. Random irregularities in turbulent fields lead to random scatterings. The resulting motion of charged particles may therefore be called a random walk in pitch angle scattering (see Longair 2011).

The theoretical framework describing the interaction of highly energetic particles moving in partially ionized, magnetoactive plasmas is called magnetohydrodynamics (MHD). This theoretical framework is to be applied when analyzing the diffusion of cosmic rays in a magnetized surrounding. Here, particles are scattered randomly on magnetohydrodynamic waves (e.g. Alfvén waves) and discontinuities which arise in response to perturbations. This means that the irregularities charged particles scatter off may be a result of their own interaction with their surrounding. A short introduction to this topic is given in Strong et al. (2007), and references to more sophisticated literature on the theory of cosmic ray diffusion can be found therein. Following the presentation of Strong et al. (2007), the *spectral energy density*  $\omega$  of magnetic interstellar turbulence, i.e. turbulent magnetic fields composed of magnetohydrodynamic waves, is given by a power-law form:

$$\omega(k) dk \propto k^{-\Gamma} dk , \quad (3.5)$$

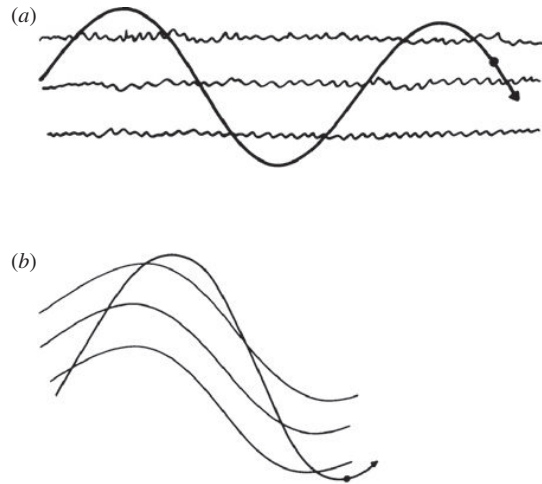


**Fig. 3.2:** *Illustration of a particle movement in irregular magnetic fields. a) Fluctuations are on a scale much smaller than the gyroradius of the particle. b) Fluctuations are on the same scale as the gyroradius of the particle (resonant pitch angle scattering). The picture is taken from Longair (2011).*

where  $k$  denotes the wave number and  $\Gamma$  the spectral index of the power law. A typical value for the spectral index is given by  $\Gamma = 5/3$ , referring to a Kolmogorov-type spectrum, whereas a spectral index of  $\Gamma = 3/2$  or  $\Gamma = 1$  refers to Kraichnan or Bohm turbulence. These different values represent different turbulence models, which are typically proposed in the context of diffusion of cosmic rays in the interstellar medium or in giant molecular clouds (see for example Fatuzzo et al. 2010).

If the gyroradii of particles are much smaller than the scale of the fluctuations, particles simply follow the magnetic field lines in their small-scale environment. In the other extreme limit, when the gyroradius is much larger than the scale of the fluctuations, the particle orbit is determined by the mean magnetic field, meaning that it is not affected by the fine field structure. Thus, the described wave-particle interaction exhibits a resonant character: only if the gyroradius of particles is at the same scale as the fluctuations in the magnetic field, there is a significant scattering. This is illustrated in Fig. 3.2. In the resonant case, the pitch angle of a particle can significantly change in a single gyration. The random superposition of such fluctuations like the superposition of MHD-waves, generating turbulent magnetic fields, leads to stochastic changes in pitch angles, which, in turn, leads to the already mentioned random walk behavior (Longair 2011). Turning from the microscopic description to a macroscopic point of view, it is commonly known that random walk behavior leads to diffusion regarding a statistical description of an ensemble of particles. This topic is addressed in the following section.

### 3.1.2 Diffusion of cosmic rays

As motivated in the previous sections, high-energy particles are assumed to diffuse away from their power source due to their interactions with turbulent magnetic fields. Therefore, a statistical treatment of the problem is given by the solution of the diffusion equation, which will be derived in the following.

Neglecting energy losses or gains and a time-dependent influence of particle injection by the source, i.e. an explicit time dependent source term  $Q(E, \mathbf{r}, t)$ , a time dependent change in the number density of particles  $n(E, \mathbf{r}, t)$  is caused by a spatial change in the flux of particles  $\mathbf{j}(E, \mathbf{r}, t)$ :

$$\frac{\partial n(E, \mathbf{r}, t)}{\partial t} = -\nabla \mathbf{j}(E, \mathbf{r}, t) . \quad (3.6)$$

Here,  $E$  denotes the energy of the particles. The diffusion assumption per definition holds the relation

$$\mathbf{j}(E, \mathbf{r}, t) = -D(E, \mathbf{r}, t) \nabla n(E, \mathbf{r}, t) , \quad (3.7)$$

meaning that the spatial flux of particles is related to the spatial gradient of particle density via the diffusion coefficient  $D(E, \mathbf{r}, t)$ . Hence, assuming scalar, constant diffusion  $D(E, \mathbf{r}, t) = D(E)$ , the diffusion equation is given by

$$\frac{\partial n(E, \mathbf{r}, t)}{\partial t} = D(E) \nabla^2 n(E, \mathbf{r}, t) . \quad (3.8)$$

Supposed that at time  $t = 0$ ,  $N_0$  particles are ejected by a source located at the origin, the solution of the diffusion equation is given by (see e.g. Bakunin 2008)

$$n(E, \mathbf{r}, t) = \frac{N_0}{[4\pi D(E)t]^{3/2}} \exp\left(-\frac{r^2}{4D(E)t}\right) . \quad (3.9)$$

Accordingly, the quantity  $(n(E, \mathbf{r}, t)/N_0) d^3r$  gives the probability of finding an injected particle at time  $t$  in a volume  $d^3r$  at position  $\mathbf{r}$ . That means the probability density function (PDF) for the spatial distribution of the particles as a function of time is obtained by normalizing to the number of injected particles. The marginal PDF  $f(r_i)$  along each of the three spatial axes ( $r_i = x, y, z$ ), calculated from the solution given by Eq. 3.9, is a Gaussian distribution

$$f(r_i) = \frac{1}{\sqrt{2\pi\sigma^2}} \exp\left(-\frac{r_i^2}{2\sigma^2}\right) \quad (3.10)$$

with a mean of  $\mu = 0$  and a width of  $\sigma = [2D(E)t]^{1/2}$ . This result is a characteristic attribute of diffusion processes. The only quantitative information about the movement of particles is given by the standard deviation, since particles diffuse away in all directions and therefore the mean value is zero. Concerning the interpretation of the movement of a single particle, one can say that the mean distance a particle travels away from its source in a certain direction is given by the standard deviation  $\sigma$ , which is proportional to the square root of time:  $\sigma \propto \sqrt{t}$ . Therefore, the output measures used for a numerical analysis of the dynamics of an ensemble of charged particles in turbulent magnetic fields, presented within the next sections, are the standard deviations of the distributions of the positions of the particles along the three spatial axes.

## 3.2 Simulating particle propagation by ensemble tracking

In this section, the method used for a numerical simulation of charged-particle motion in turbulent magnetic fields is presented. Throughout this work, particles are treated as test particles, meaning that their motion has no influence on the configuration of the magnetic field. First, a description of the numerical procedure used to generate turbulent magnetic fields is given. In the following, this procedure is used for tracking particles through turbulent magnetic fields. The tracking of single particles is presented before turning to an analysis of the movement of an ensemble of particles and defining the output measures that characterize this movement. Afterwards, the influence of different parameters on the results of the simulation is tested.

### 3.2.1 Modeling of the turbulent magnetic field

For setting up a turbulent magnetic field, an approach introduced by Giacalone & Jokipii (1994) is adopted. The formalism presented in this pioneering work has already been used by other authors (e.g. Wommer et al. 2008; Fatuzzo et al. 2010) and is very similar to the approach of several other authors numerically investigating ionic motion in turbulent magnetic fields (e.g. Casse et al. 2002; O’Sullivan et al. 2009).

Following Giacalone & Jokipii (1994), the total magnetic field  $\mathbf{B}(\mathbf{r})$  is written as the sum of two terms: a static background component  $\mathbf{B}_0$  superimposed by a spatially fluctuating component  $\delta\mathbf{B}(\mathbf{r})$ . A three dimensional realization of  $\delta\mathbf{B}(\mathbf{r})$ , which satisfies Gauss’s law  $\nabla \cdot \mathbf{B} = 0$ , is given by the sum over a large number  $N$  of randomly polarized transverse waves

$$\delta\mathbf{B}(\mathbf{r}) = \sum_{n=1}^N B_n \left[ \cos \alpha_n \hat{x}' \pm i \sin \alpha_n \hat{y}' \right] \times \exp \left[ ik_n z' + i\beta_n \right] \quad (3.11)$$

where  $\alpha_n$  and  $\beta_n$  are random numbers between 0 and  $2\pi$ . The values of the wave numbers  $k_n$  are evenly spaced on a logarithmic scale between  $k_1 = 2\pi/\lambda_{\max}$  and  $k_N = 2\pi/\lambda_{\min}$ , which refer respectively to the maximum and minimum wavelength  $\lambda$  of the turbulent field. A random choice of  $\pm$  selects the helicity of the wavevector  $\mathbf{k}_n$  about the  $z'$  axis. The unprimed system (laboratory frame) is related to the primed system via the rotation matrix

$$\mathbf{R} = \begin{pmatrix} \cos \theta_n \cos \phi_n & -\sin \phi_n & \sin \theta_n \cos \phi_n \\ \cos \theta_n \sin \phi_n & \cos \phi_n & \sin \theta_n \sin \phi_n \\ -\sin \theta_n & 0 & \cos \theta_n \end{pmatrix}, \quad (3.12)$$

where  $0 \leq \phi_n \leq 2\pi$  and  $0 \leq \theta_n \leq \pi$  are randomly selected angles defining the direction of  $\mathbf{k}_n$ . Therefore, 5 random numbers are needed in total for each value of  $n$ . The requested spectrum of the irregular component is obtained by the corresponding choice of  $\Gamma$  in the scaling

$$B_n^2 = B_1^2 \left[ \frac{k_n}{k_1} \right]^{-\Gamma+1}, \quad (3.13)$$

where  $\Gamma = 5/3$  refers to Kolmogorov,  $\Gamma = 3/2$  to Kraichnan and  $\Gamma = 1$  to Bohm turbulence as described in Section 3.1.1. In the initial work of Giacalone & Jokipii (1994), only Kolmogorov turbulence was considered. But as all three models assume a power law scaling, only with different spectral indices, the formalism is simply generalized. The value of  $B_1$  is determined by the demand that there is as much energy density contained in the turbulent magnetic field as there is in the static component. Taking into account

the relation  $S \propto \mathbf{B}^2$ , with  $S$  the total energy density of the magnetic field, one obtains the relation

$$B_1^2 \sum_n \left[ \frac{k_n}{k_1} \right]^{-\Gamma+1} = 2B_0^2 . \quad (3.14)$$

Here, it is assumed that there is a sufficient large number of randomly polarized waves in the turbulent component  $\delta\mathbf{B}$  so that the cross terms of the dot product  $[\text{Re}(\delta\mathbf{B})]^2$  average to zero.

### 3.2.2 Single particle tracking

The tracking of a single particle in a turbulent magnetic field, i.e. for this work protons, is carried out as follows. First, the turbulent magnetic field is set up following the method described in the previous section. For this purpose,  $N=200$  values of  $k$  are used, with wavelengths between 0.1 and  $10R_g$ .  $R_g$  denotes the maximum gyroradius of a proton in the homogeneous background field  $\mathbf{B}_0$ , which can be written as (Fatuzzo & Melia 2012)

$$R_g = 0.02 \text{ pc} \left( \frac{\gamma}{10^6} \right) \left( \frac{50 \mu\text{G}}{B_0} \right) , \quad (3.15)$$

using the approximation  $v \approx c$ . From now on, the quantity defined in Eq. 3.15 is addressed when referring to the particle gyroradius. Furthermore, Kolmogorov turbulence is assumed, i.e. the value of  $\Gamma$  is set to  $\Gamma = 5/3$ . The strength of the homogeneous component is set to  $B_0 = 50 \mu\text{G}$ , and its direction is chosen along the  $z$  axis,  $\mathbf{B}_0 = B_0 \mathbf{e}_z$ . The choice of this configuration orientates on that of the works of Wommer et al. (2008) and Fatuzzo & Melia (2012), and is selected as a first baseline configuration. The influence of the different parameters on the simulation is tested later on (see Section 3.2.4). The sets of 5 random numbers needed for each value of  $k_n$  are generated at the beginning of the simulation, so that the magnetic field can be calculated at each point  $\mathbf{r}$  in a three dimensional space.

Having set up the magnetic field, the tracking of a single proton is achieved by solving the equation of motion (see Eq. 3.1) for discrete time steps  $dt$ . To calculate the proton's position after each  $dt$ , a transformation to a coordinate system, in which the total magnetic field is parallel to the  $z$  axis, is performed. Then, the Lorentz force equation is solved, assuming that the magnetic field is constant over the small distance the proton travels within  $dt$ , i.e. the solution of the Lorentz force equation is known, see Eq. 3.2. A rotation back to the global coordinate system gives the current position and momentum of the particle after the time step  $dt$ . The total time a particle is followed is given by  $t = N_s dt$ , including  $N_s$  tracking steps. The choice of the time step is important to ensure accuracy for the applied method. In this work, a value of  $dt = T/200$  is applied, with  $T$  the time a particle needs for one gyration in a magnetic field of strength  $B_0$ ,

$$T = \frac{2\pi}{\omega} = \frac{2\pi\gamma m}{eB_0} , \quad (3.16)$$

where the definition of the cyclotron frequency  $\omega$  is used (see Eq. 3.4) and  $e$  denotes the elementary charge. The chosen value for the time step will be justified in Section 3.2.4, in which parameter influence is analyzed systematically.

The resulting trajectory of a 1 TeV proton injected at the origin is shown in Fig. 3.3. The expected random walk behavior, as described in Section 3.1.1, is clearly recognizable. The scale of the movement in  $z$  direction is larger than in  $x$  or  $y$  direction, respectively,

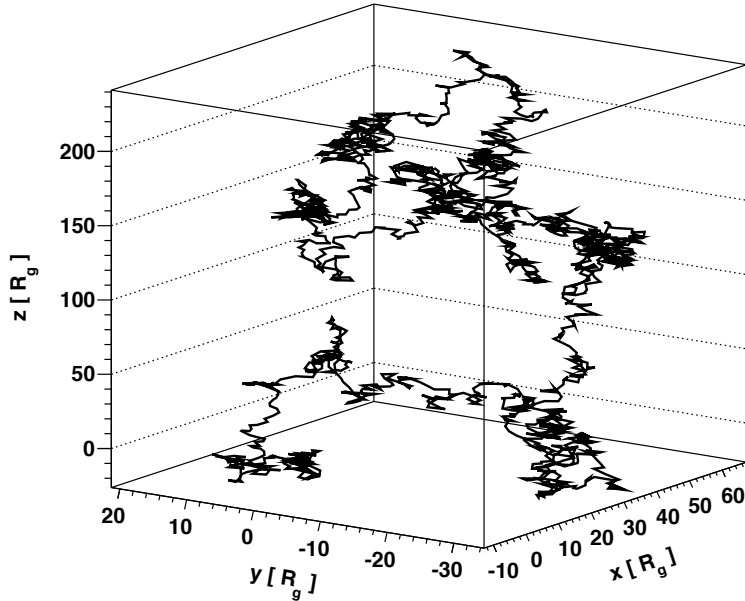


**Fig. 3.3:** Random walk trajectory of a 1 TeV proton in a turbulent magnetic field, as specified in the text. The unit of the axes is chosen as  $R_g$ , which denotes the particle's gyroradius in the homogeneous background field of strength  $B_0$  ( $R_g \approx 2.2 \times 10^{-5}$  pc for the defined value  $B_0 = 50 \mu\text{G}$ ). The influence of the static background component on the dynamics of the proton is visible in the picture, as the scale of the movement in  $z$  direction is clearly larger than the one in the  $xy$  plane. The trajectory of the proton is followed for a total time of  $1000T \approx 1.4 \times 10^8$  s, every 100th step being shown.

reflecting the influence of the homogeneous background field. The next step after the presentation of single particle treatment is a statistical analysis of the movement of an ensemble of particles. This topic is addressed in the next section.

### 3.2.3 Ensemble tracking and output measures

The procedure for the tracking of an ensemble of particles is very similar to the one for the tracking of single particles. The random numbers used for calculating the magnetic field at the positions of the individual particles are generated at the beginning just like before. Afterwards, each particle is tracked for the desired period of time. All particles are injected at the origin, and their starting velocity vectors are uniformly distributed on the surface of a sphere with a radius according to the desired energy. The number of particles used to set up an ensemble is  $N_p = 1000$  protons throughout this work. All other configurations are identical to the ones introduced in the previous section.

The resulting spatial distributions of the particles along the  $x$  and  $z$  axis are shown in Fig. 3.4, respectively. The distribution along the  $y$  direction, which is identical to the one in  $x$  direction, apart from statistical fluctuations, is not explicitly shown. In contrast, the

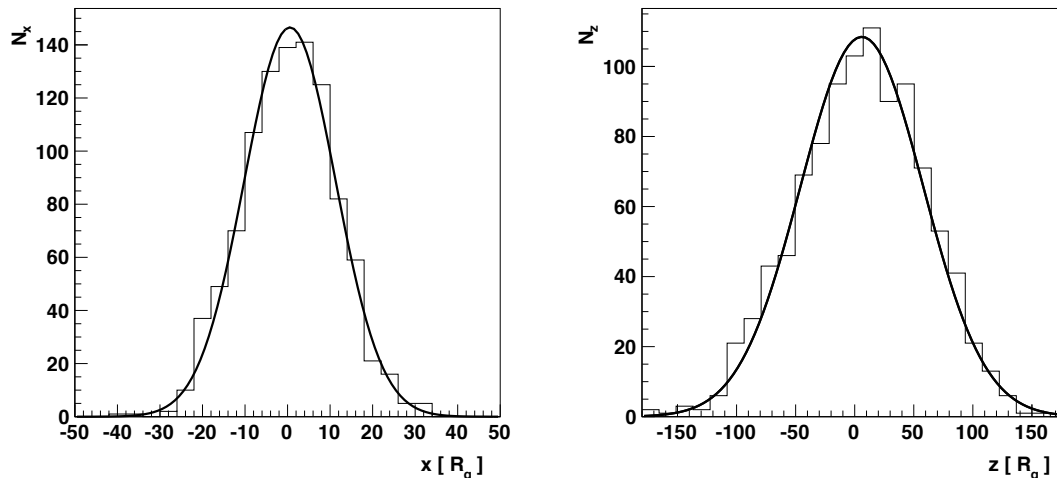


**Fig. 3.4:** Distribution of  $N_p = 1000$  protons ( $E = 1$  TeV) along  $x$  (left) and  $z$  (right) direction after a time  $t = 100T$ . The data are well described by Gaussian statistics, illustrated by the superimposed Gaussian distributions. The influence of the homogeneous background field is reflected in the different width of the distributions.

spread in  $z$  direction is, as expected, clearly larger, which again shows the influence of the homogeneous component of the magnetic field (the standard deviation in  $z$  direction is about 5 times larger than the one in  $x$  direction at  $t = 100T$ ). The results show that the diffusion process is well represented by Gaussian statistics, as illustrated by the superimposed Gaussian distributions well fitting the data. Therefore, the second part of this section deals with the time development of the width of the distributions, i.e. checking the functional relation between the standard deviation  $\sigma(t)$  and time  $t$ .

### Time development and output measures

As discussed in Section 3.1.2, the useful output measures for time analysis are the standard deviations of the spatial distributions of the particles along the three spatial axes. As primary output measure, the corrected sample standard deviation, based on the sample of  $N_p = 1000$  particles, is used. This quantity is calculated as the square root of the unbiased estimator for the sample variance and is denoted as  $\hat{\sigma}_i$  ( $i = x, y, z$ ). The final output measures used in the following are mean values  $\langle \hat{\sigma}_i \rangle$ , calculated from the single output measures  $\hat{\sigma}_{n,i}$  ( $n \in \{1, \dots, 50\}$ ) of 50 runs of the simulation with identical settings,

$$\sigma_i := \langle \hat{\sigma}_i \rangle = \frac{1}{50} \sum_{n=1}^{50} \hat{\sigma}_{n,i} \quad , \quad (3.17)$$

which are denoted as  $\sigma_i$  for a simplification of notation. These quantities allow an analysis of statistical influences, as one can estimate an error  $\delta\sigma_i$  for the quantity  $\sigma_i$ , calculated via the corrected sample standard deviation based on the set of the 50 values for  $\hat{\sigma}_{n,i}$  (see Section 3.2.4).

The settings of the magnetic field and the particle energy ( $E = 1$  TeV) are again identical to the ones used before. The resulting values of  $\sigma_x$  and  $\sigma_z$  as a function of time are shown

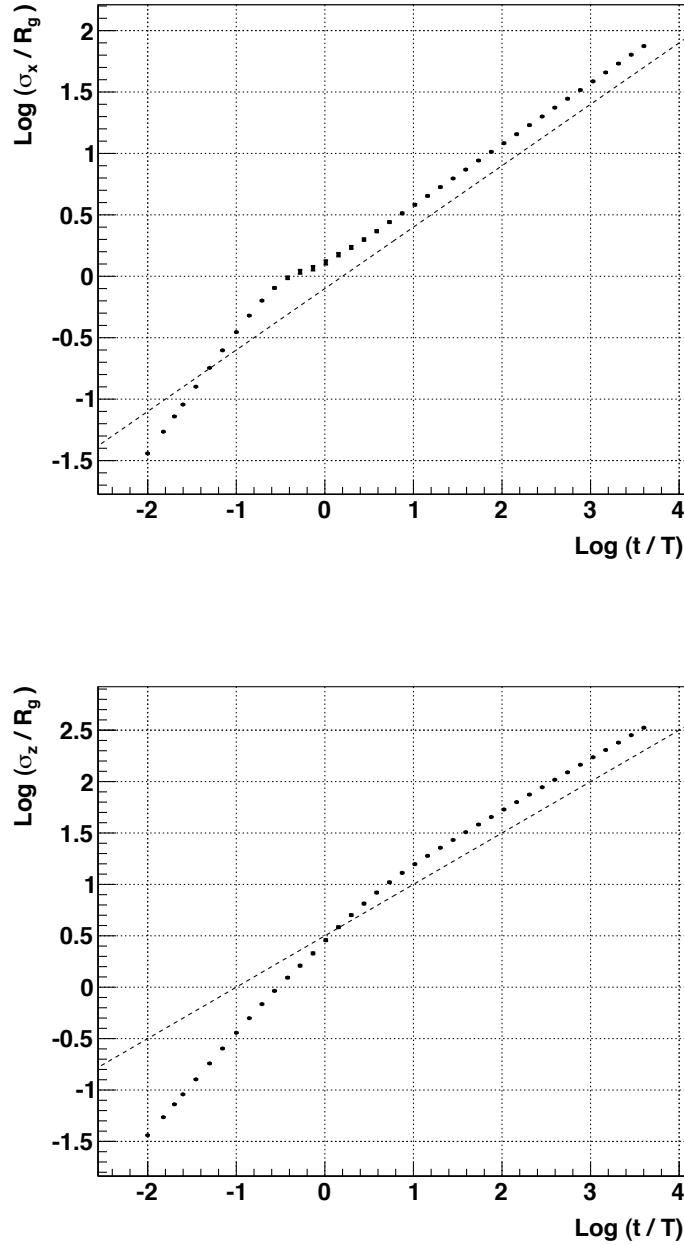


**Fig. 3.5:** Standard deviation  $\sigma_i$  (see text) of the spatial distribution of the particles in  $x$  and  $z$  direction as a function of time. The dashed line has a slope of  $1/2$  and serves as reference. Once particles have fully sampled the turbulent structure of the field ( $t \approx \lambda_{\text{max}}/c$  or  $\text{Log}(t/T) \approx 0.2$  for the chosen settings), the time development of the quantities is proportional to the square root of time:  $\sigma_{x,z} \propto \sqrt{t}$ .

in Fig. 3.5. A break in the slope of the curves from  $\sim 1$  to  $1/2$  is visible for both output measures, indicating that particles have fully sampled the turbulent structure of the field at  $t \approx \lambda_{\max}/c$ , corresponding to a value of  $\text{Log}(t/T) \approx 0.2$  for the chosen settings. This time is approximately equal to the time a particle needs to traverse the spatial scale of the maximum wavelength of the turbulent field. Such a break has already been observed at the same point in time within the analysis of other authors, e.g. Fatuzzo et al. (2010) or Fatuzzo & Melia (2012), showing consistency with this analysis.

Summed up, the results show the expected time development  $\sigma \propto \sqrt{t}$  as discussed in Section 3.1.2, once particles have reached the turbulent regime. The values along the y direction are not shown explicitly, but were cross-checked. As expected, they show very good agreement with the corresponding values along x direction (within the estimated errors  $\delta\sigma_i$ ). Relative errors  $\delta\sigma_i(t)/\sigma_i(t)$  are constant once particles have reached the turbulent regime. The values are  $\sim 0.01$  in x and y direction, respectively, and  $\sim 0.005$  in z direction. Now that first results of the simulation have been shown, the following section presents the analysis of the influence of specific parameter values, which need to be specified in the used formalism.

### 3.2.4 Influence of model parameters

In the numerical approach used here, the values of different parameters need to be specified. The choice of appropriate values is on the one hand important to ensure accuracy of the applied formalism, like the choice of a specific value for the tracking time step  $dt$ . On the other hand, the influence of the chosen values for parameters with a more physical background on the results of the simulation might be of interest, e.g. assigning a specific value to the spectral index of the power spectrum of the turbulent field. The determination of the used value for the time step  $dt$  will be discussed in the following. The influence of the specification of other parameter values was analyzed within the Bachelor thesis of M. Oberndörfer, and only a short review of these results will be given here. For a more detailed discussion, see Oberndörfer (2014).

The strength of parameter influences on the results of the simulation can be estimated by an analysis of the variance of the single output measures  $\hat{\sigma}_i$  ( $i = x, y, z$ ). Therefore, the corrected sample standard deviation, based on the 50 simulation runs with identical settings, is calculated:

$$\sigma_{\sigma,i} = \sqrt{\frac{1}{50-1} \sum_{n=1}^{50} (\hat{\sigma}_{n,i} - \sigma_i)^2} . \quad (3.18)$$

An error of the mean value  $\sigma_i$  is accordingly calculated as  $\delta_i = \sigma_{\sigma,i}/\sqrt{50}$ . Unless otherwise specified, in the following, all parameter values are set to the baseline configuration used until here: particle energy  $E = 1$  TeV, wavelength interval  $0.1 - 10R_g$  including  $N = 200$  values of  $k$ , strength of the homogeneous background field  $B_0 = 50 \mu\text{G}$  and a tracking time step of  $dt = T/200$ .

#### Choice of the tracking time step $dt$

An appropriate choice of the value of the tracking time step  $dt$  is important to ensure accuracy for the applied formalism, meaning that  $dt$  should be chosen as small as possible. However, small time steps result in large computing time. Therefore, a set of experiments was performed to determine an optimal value, without sacrificing accuracy. As natural

time scale serves the time  $T$ , defined as the time a particle needs for one gyration in a magnetic field of the strength of the homogeneous background field (see Eq. 3.16). The systematics of the shown results are identical in each direction, so that a discussion can be restricted to the x direction. The shown data points refer to the turbulent regime, meaning that particles have already completely sampled the turbulent structure of the magnetic field.

The results for different time steps  $dt = T/x$ , with  $x = 25, 50, 100, 200$  are shown in Fig. 3.6. The values of  $\sigma_x$  as a function of time show differences, but these are small compared to the spread of the single output measures  $\hat{\sigma}_x$ , estimated by the sample standard deviation  $\sigma_{\sigma,x}$ , as shown on the right hand side of Fig. 3.6. Irregularities in the time development of the quantity  $\sigma_{\sigma,x}$ , visible for all different time steps, are of statistical nature. As a time step of  $dt = T/200$  turns out to be a computationally feasible value, the choice of this value was tested against a value of  $dt = T/1000$ . The output measure  $\sigma_x$  is for both time steps shown in Fig. 3.7 on the left hand side. Only very small differences in the time development of the values are observable. Their relative difference, given in the bottom panel, is constant over time with an average value of 0.010, indicated by the dashed line. The calculated sample standard deviations are shown on the right hand side of Fig. 3.7, together with the corresponding relative values in the bottom panel. The relative values are constant in time and are both about 0.075. Therefore, a tracking time step of  $dt = T/200$  is assumed to provide good accuracy in the results and is applied for all following simulations.

### **Influence of different values for the spectral index $\Gamma$**

The analysis of the influence of a specific choice of the value of the spectral index  $\Gamma$  of the power spectrum of the turbulent magnetic field on the output of the simulation was performed within the Bachelor thesis of M. Oberndörfer (2014). The analysis considered the three different values for Kolmogorov, Bohm and Kraichnan turbulence. The deviation in the output measures  $\sigma_i$  was tested for Bohm and Kraichnan turbulence against a Kolmogorov type spectrum, respectively. The results show differences smaller than 3% in x or y direction and smaller than 1% in z direction, once particles have reached the turbulent regime. The spread of values, calculated with Kolmogorov turbulence, is clearly larger being  $\sigma_{\sigma,x}/\sigma_x \approx \sigma_{\sigma,y}/\sigma_y \approx 7.5\%$  and  $\sigma_{\sigma,z}/\sigma_z \approx 3.5\%$ . Therefore, no significant influence for the choice of a specific value is observed, and the analysis of this work is restricted to Kolmogorov turbulence.

### **Influence of the number of transverse waves $N$ used to set up $\delta\mathbf{B}$**

An important question is which value of  $N$ , the number of transverse waves used to set up the turbulent component of the magnetic field  $\delta\mathbf{B}$ , is a suitable choice to represent the continuous fields found in nature. A short test regarding this issue was also carried out within the thesis of Oberndörfer (2014). The value of  $N$  was changed from  $N = 200$  to  $N = 300$  wave vectors. The position and length of the wavelength interval of the turbulent field was changed within this analysis, too. This point will be discussed in the next paragraph. The results for a constant position and length of the wavelength interval showed very small differences in the output measures  $\sigma_i$ , compatible with the calculated errors  $\delta\sigma_i$ , when switching the value  $N = 200$  to  $N = 300$ . A more extended study, e.g. choosing  $N = 1000$ , was not performed due to intensive computing time. The discussed result indicates that the setting  $N = 200$  provides good accuracy. The value  $N = 200$  is identical to that used by Wommer et al. (2008), and is 8 times higher than the one used in the analysis of Fatuzzo & Melia (2012).

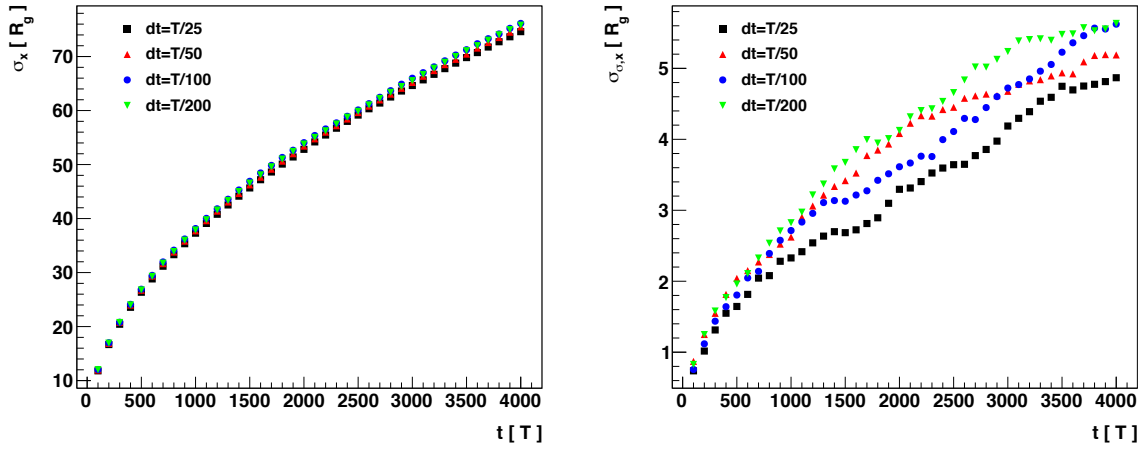


**Fig. 3.6:** Output measure  $\sigma_x$  (left) and estimated standard deviation  $\sigma_{\sigma_x}$  (right) as a function of time for various time steps  $dt$ . Differences in the values of  $\sigma_x$  for different time steps are visible, but small compared to the spread of single values estimated by the quantity  $\sigma_{\sigma_x}$ . Irregularities in the time development of the quantity  $\sigma_{\sigma_x}$ , visible for all time steps, are of statistical nature.

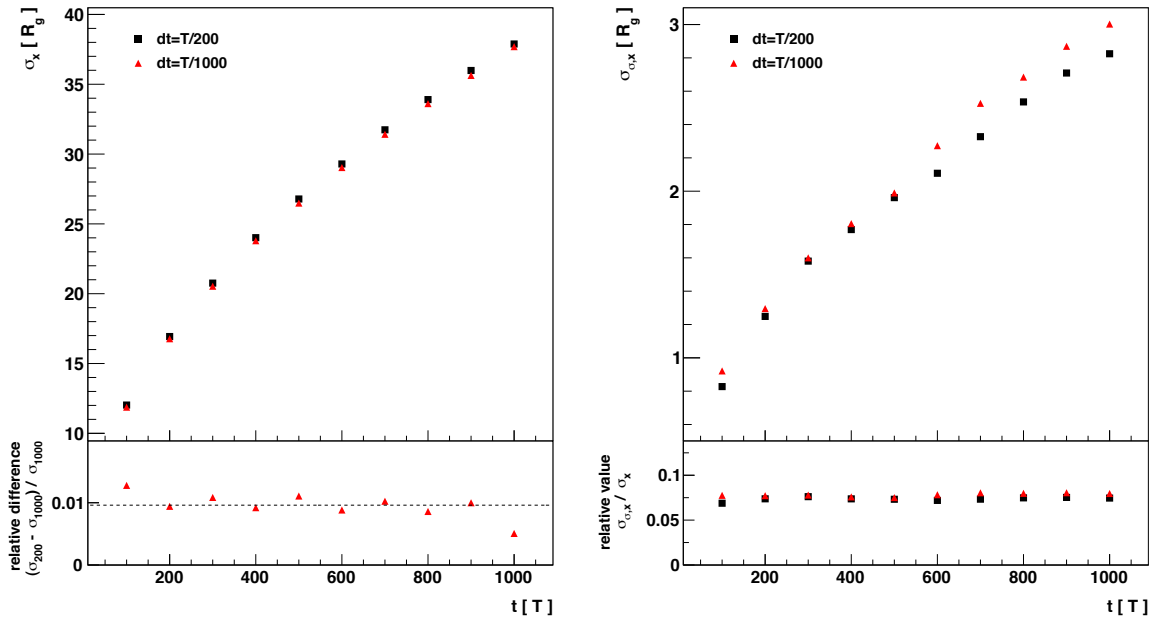


**Fig. 3.7:** Output measure  $\sigma_x$  (left) and estimated standard deviation  $\sigma_{\sigma_x}$  (right) as a function of time for the time steps  $dt = T/200$  and  $dt = T/1000$ . The relative difference of the values of  $\sigma_x$  is 0.010 on average, indicated by the dashed line (bottom panel left side). The relative value for the estimated standard deviations is about 0.075, respectively (bottom panel right side). Therefore, a value of  $dt = T/200$  is expected to provide good accuracy in the results of the simulation.

**Influence of the values chosen for the minimum and maximum turbulent wavelength (position of  $\lambda_{\min}$  and  $\lambda_{\max}$ )**

The choice of the value of the maximum and minimum wavelength used to set up the turbulent magnetic field with respect to the particles' gyroradius  $R_g$  is important as the scattering of particles off the turbulent field is of resonant character (see Chapter 3.1.1). The value of the minimum turbulent wavelength has no significant influence on the time development of the output measure  $\sigma_i$ , as long as  $R_g > \lambda_{\min}$ , as shown by Fatuzzo et al. (2010). Therefore, a value of  $\lambda_{\min} = 0.1R_g$  is used for all simulations throughout this work. In contrast to this, the choice of the value for the maximum turbulent wavelength  $\lambda_{\max}$  is expected to show a considerable influence on the output measures  $\sigma_i$ , as the power spectrum of the turbulent field scales down with a power law. Hence, more power is given to wavelengths in the upper end of the interval, compared to those in the lower end. A systematic study of this influence on the results of the simulation was presented in the Bachelor thesis of Oberndörfer (2014). While keeping  $\lambda_{\min} = 0.1R_g$  constant, the value of  $\lambda_{\max}$  was varied within a range between  $10R_g$  and  $1000R_g$ . As expected, the output measures  $\sigma_i$  showed significant differences. Diffusion coefficients, calculated from the time development of the quantities  $\sigma_i$  show differences of approximately one order of magnitude when varying the value of the maximum turbulent wavelength from  $10R_g$  up to  $1000R_g$  (see supplementary Fig. A.1).

Summed up, the analysis of parameter influence shows that the dynamics of charged particles in turbulent magnetic fields are, for the applied formalism, only strongly influenced by a single parameter - the value of the maximum turbulent wavelength  $\lambda_{\max}$  with respect to the gyroradius  $R_g$  of the particles. This result is consistent with the analysis of Fatuzzo et al. (2010). These authors name the ratio of the turbulent to uniform magnetic field energy densities as a second important parameter. Within this work, this ratio is treated as a constant, so that these energy densities have the same value. Influences caused by a variation of the magnetic field strength  $B_0$  are not explicitly analyzed. A change of this quantity is only a scaling problem, since changing its value means changing the value of the gyroradius  $R_g$ . No new relevant knowledge could be gained with respect to a dimensionless analysis. The aim of the following sections is to derive diffusion coefficients as a function of energy for a constant magnetic field configuration. The results of this section will thereby be used to apply the established formalism numerically adequate on the assumed environmental conditions of the Galactic Center region.

### 3.3 Application to the Galactic Center region

In this section, the introduced numerical formalism for a simulation of charged-particle motion in turbulent magnetic fields is applied to the environmental conditions of the Galactic Center region. Section 3.3.1 deals with a discussion of these conditions and an appropriate setting of corresponding basic simulation parameters. In Section 3.3.2, diffusion coefficients as a function of energy are derived from the output measures of numerical particle tracking. This implies an analysis of the energy dependence of the diffusion coefficient for a constant magnetic field configuration, chosen according to the discussed conditions. The diffusion coefficients will serve as input parameters for long-distance particle tracking within the modeling of diffuse  $\gamma$ -ray emission from the Galactic Center region, see Chapter 4.1.

### 3.3.1 Environmental conditions and parameter settings

A large concentration of dense molecular gas ( $\sim 10^8 M_\odot$ ), concentrated in so-called Giant Molecular Clouds with sizes of approximately 50 – 70 pc, characterizes the environment in the central region of the Galactic Center. The size of this so-called Central Molecular Zone is about  $450 \times 50$  pc, and its center is  $\sim 2/3$  shifted towards positive longitudes (Güsten & Philipp 2004). The density distribution is mapped using density-sensitive molecular species, e.g. CS (Bally et al. 1987),  $\text{H}_2\text{CO}$  (Guesten & Henkel 1983) or  $\text{HC}_3\text{N}$  (Walmsley et al. 1986). Such excitation surveys propose that the Galactic Center clouds contain high density clumps ( $\sim 10^5 \text{ cm}^{-3}$ ) embedded in a surrounding of lower density ( $\sim 10^{3.7} \text{ cm}^{-3}$ ), see e.g. Walmsley et al. (1986). The average gas density is then approximately  $\langle n \rangle \sim 10^4 \text{ cm}^{-3}$ . An overview of more recent mm/submm line surveys of the Galactic Center region can be found in Güsten & Philipp (2004). One of the most complete measurements so far is given by the CS(1-0) mapping of the area with the NRO telescope (Tsuboi et al. 1999). This measurement was used to set up the density map of the Galactic Center molecular clouds used in this work, see Section 4.1.2.

Turning to the Galactic Center magnetosphere, the situation is much more complicated. Local observations of Non-thermal Filaments (NTFs) in radio continuum images can be seen as striking manifestation of the magnetic field in the interstellar medium of the Galactic Center region (e.g. Yusef-Zadeh et al. 1984). These NTFs run roughly perpendicular to the Galactic plane, with a length of tens of parsecs, while their transverse structure is restricted to only a fraction of a parsec. Thus, the observations of NTFs suggest a poloidal field structure with a strength of a few mG (see Güsten & Philipp 2004; Ferrière 2009). Further radio observations, like Zeeman splitting measurements, however, tend to point to smaller values for the interstellar magnetic field strength, resulting in an uncertain range from  $\sim 10 \mu\text{G}$  up to  $\sim 1 \mu\text{G}$  (Ferrière 2009). Additional information is given by mid- and far-infrared thermal dust emission from magnetically aligned dust grains inside the molecular clouds. Such observations suggest magnetic fields of toroidal structure, parallel to the Galactic plane (see Güsten & Philipp (2004), Ferrière (2009) and included references). Chuss et al. (2003) found a connection between measured field direction and the density of surrounding material in their data, suggesting that the field is generally parallel to the Galactic plane in high-density regions, while in regions of lower density it is generally perpendicular to it. As possible explanation for such a co-existing poloidal and toroidal magnetic field structure, the authors propose an interaction between gravitational forces of the dense clouds and magnetic forces, so that an originally poloidal configuration is sheared into a toroidal configuration.

In summary, the exact structure of the large-scale magnetic field in the Galactic Center region is not well understood, and there is no general agreement on the magnetic field strength estimated from different experimental observations. A lower limit of  $50 \mu\text{G}$  for the magnetic field strength in the Galactic Center region was recently given by Crocker et al. (2010), inferred from an analysis of its non-thermal radio spectrum.

The Galactic Center region is also known to show strong turbulence activity. According to Boldyrev & Yusef-Zadeh (2006), the fluctuating part of the field should be of the same order as its large-scale component. Turning to an extended description of the uncertainties of the magnetic field, these authors suggest a turbulent origin for the NTFs and for the Galactic Center large-scale field itself. In such a picture, the spatial distribution of magnetic field energy is highly intermittent, and magnetic enhanced regions would be associated with the observed NTF-structures (see Boldyrev & Yusef-Zadeh 2006).

Basic parameters of the numerical simulation, which need to be arranged according to the described conditions, are the maximum turbulent wavelength  $\lambda_{\max}$  and the strength of the uniform magnetic field  $B_0$ . For the latter, two different values of  $B_0 = 50/500 \mu\text{G}$  are adopted in agreement with the lower limit given by Crocker et al. (2010). Furthermore, as there is no conclusive picture of the entire magnetic field configuration, the diffusion coefficients in the next section will be derived under the assumption of a turbulent magnetic field superimposed by a static component of strength  $B_0$ , as before, and under the assumption of a purely turbulent magnetic field. This simply means to remove the static background component from the formalism. The energy density of the purely turbulent field is thereby assumed to be equal to that of a homogeneous field of strength  $B_0$ . The approach of working with a purely turbulent field in a numerical formalism as used in this work has already been used by Fatuzzo et al. (2010), analyzing cosmic-ray diffusion in molecular clouds in general. According to these authors, the value of  $\lambda_{\max}$  is not known for molecular cloud environments, but a reasonable assumption would be that it is constrained from below by the size of dense cores,  $\sim 0.1 \text{ pc}$ , and from above by the actual size of the entire clouds, a few tens of parsecs. Therefore, following Fatuzzo et al. (2010), an intermediary value of  $\lambda_{\max} = 1 \text{ pc}$  will be used. This value was also used by Fatuzzo & Melia (2012), assessing the feasibility of stochastic particle acceleration at the Galactic Center.

After having discussed environmental conditions and having determined basic parameters according to these, the next section deals with a derivation of diffusion coefficients. A more general overview on the application of the numerical simulation will be given there.

### 3.3.2 Extraction of diffusion coefficients

As described above, diffusion coefficients will be derived from the results of the numerical simulation for the case of both a turbulent magnetic field superimposed by a static background component (defined to point along the  $z$  direction) and a purely turbulent field. The choice of the field strength  $B_0 = 50/500 \mu\text{G}$  is identical to the setting in the analysis of Fatuzzo & Melia (2012), as well as the choice of  $\lambda_{\max} = 1 \text{ pc}$ . This allows a comparison of results. Specifying further simulation settings,  $N = 200$  values of  $k$  are used, together with a time step of  $dt = T/200$ . The minimum turbulent wavelength is set to  $\lambda_{\min} = 0.1 R_g$  (again identical to the settings of Fatuzzo & Melia 2012). These quantities are calculated according to the adjusted particle energy  $E$ . Considered energies  $E$  lie within a range of  $13 \leq \text{Log}(E/\text{eV}) \leq 15.5$  for  $B_0 = 50 \mu\text{G}$  and  $14 \leq \text{Log}(E/\text{eV}) \leq 16.5$  for  $B_0 = 500 \mu\text{G}$ . As for all considered energies  $\lambda_{\max} > 10 R_g$ , the choice  $dt = T/200$  is assumed to provide good accuracy. In the following, the derivation of diffusion coefficients is systematically described.

For each value of adopted energy  $E$ , the primary output measures from the numerical simulation are the quantities  $\hat{\sigma}_i$ , defined as the standard deviations of the distributions of the particles' positions along the spatial axes  $i = x, y, z$ . These are calculated from the tracking of  $N_p = 1000$  particles. The particles are followed for a total time of  $4000 T$ . 50 simulation runs are performed for each energy value, giving a set of 50 primary output measures  $\hat{\sigma}_{n,i}$  ( $n \in \{1, \dots, 50\}$ ). The time development of each of these quantities is fitted according to the expected relation  $\sigma = \sqrt{2Dt}$  (see Section 3.1.2), resulting in a set of 50 estimated values  $\hat{D}_{n,i}$  for the diffusion coefficient along each spatial axis  $i$ . The lower fit boundary is set to the constant value  $t = \lambda_{\max}/c$ , assuming particles have fully sampled the turbulent structure of the field at this point in time. For each energy  $E$ , the

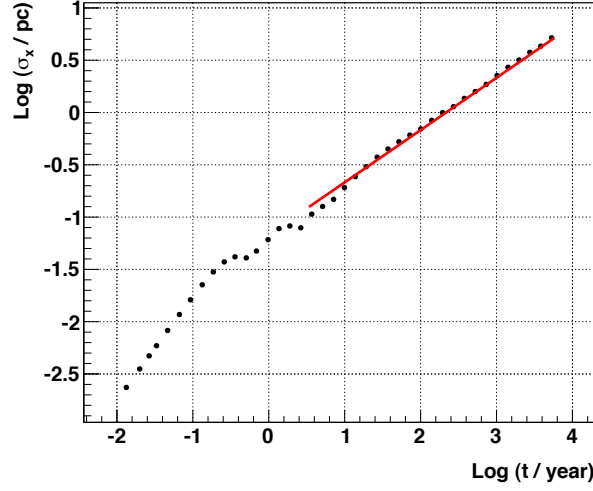


**Fig. 3.8:** Time development of the single output measure  $\hat{\sigma}_{1,x}$  for a particle energy of  $E = 3 \times 10^{15}$  eV and a magnetic field strength of  $B_0 = 50 \mu\text{G}$ . The red line shows the fit to the data according to the expected time evolution  $\sigma = \sqrt{2Dt}$ . The lower fit boundary is set to  $t = \lambda_{\text{max}}/c$  ( $\sim 0.51$  on the shown log-scale for  $\lambda_{\text{max}} = 1$  pc). The result of the fit gives a diffusion coefficient of  $\hat{D}_{1,x} = 2.3 \times 10^{-3} \text{pc}^2/\text{yr} = 6.9 \times 10^{26} \text{cm}^2/\text{s}$ .

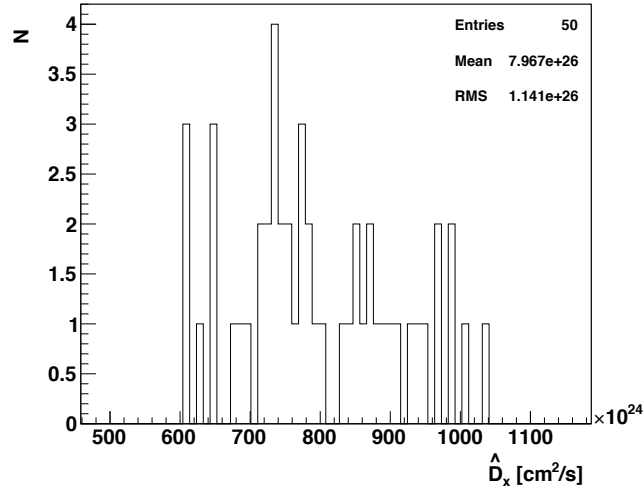


**Fig. 3.9:** Distribution of the 50 single output measures  $\hat{D}_{n,x}$  for a particle energy of  $E = 3 \times 10^{15}$  eV and a magnetic field strength of  $B_0 = 50 \mu\text{G}$ . The mean value of this distribution is taken as output measure for the diffusion coefficient along the  $x$  axis for the given settings. An error for this quantity is estimated using the sample standard deviation of the distribution, which is denoted as RMS in the plot. For this case, the result is given as  $D_x = (8.0 \pm 0.2) \times 10^{26} \text{cm}^2/\text{s}$ .

output measure for the diffusion coefficient along each spatial direction  $i$  is defined as the mean value  $\langle D_i \rangle$  of the 50 fit values. An error of these mean values is calculated via the sample standard deviation of the 50 data points. The procedure is illustrated in Fig. 3.8 and Fig. 3.9, showing an exemplary fit and a histogram of the single output measures.

For these data points, the particle energy was set to  $E = 3 \times 10^{15}$  eV, using a turbulent magnetic field superimposed by a static component.

The final output measures for the diffusion coefficients of a given particle energy  $E$  and magnetic field strength  $B_0$  are defined as follows. For the case of a turbulent field superimposed by a static background component, the mean value of the output measures along the x and y direction is calculated. This quantity is denoted as  $D_{\perp}$ . The static background component was defined to point along the z direction. Hence, the output measure along the z direction is denoted as  $D_{\parallel}$ . For the case of a purely turbulent field, the mean value of the output measures along all three spatial axes is taken as the final output measure, denoted by  $D$ . Thus, a set of six energy dependent quantities is the final result of the simulations:  $D_{\perp}(E)$  and  $D_{\parallel}(E)$ , referring to the case of taking into account a homogeneous background component, and  $D(E)$  for the case of a purely turbulent field. All quantities are calculated for  $B_0 = 50 \mu\text{G}$  and  $B_0 = 500 \mu\text{G}$ , respectively. First, a discussion of the diffusion coefficients  $D_{\perp}(E)$  and  $D_{\parallel}(E)$  will be given. These data can be compared with the diffusion coefficients calculated by Fatuzzo & Melia (2012) also working with a homogeneous background component. Afterwards, the case of a purely turbulent magnetic field will be presented.

### **Turbulent field superimposed by a static background component**

The derived diffusion coefficients  $D_{\perp}(E)$  and  $D_{\parallel}(E)$  for  $B_0 = 50 \mu\text{G}$  and  $B_0 = 500 \mu\text{G}$  are shown in Fig. 3.10 and Fig. 3.11. The blue data points are the values derived by Fatuzzo & Melia (2012) and are shown for comparison. The energy dependence of the diffusion coefficient is usually assumed to follow a power law (see e.g. Aharonian & Atoyan 1996; Fatuzzo et al. 2010; Nekrassov 2010)

$$D(E) = D_{10} \left( \frac{E}{10 \text{ GeV}} \right)^{\delta}, \quad (3.19)$$

where  $D_{10}$  denotes the the value of the diffusion coefficient at  $E = 10$  GeV. According to the standard theory for particle diffusion, the index  $\delta$  of Eq. 3.19 is related to the spectral index of the turbulent magnetic field  $\Gamma$  via the expression  $\delta = 2 - \Gamma$  (Fatuzzo et al. 2010), setting  $\delta = 1/3$  in case of Kolmogorov turbulence ( $\Gamma = 5/3$ ). In general, a value of  $\delta \sim 0.3 - 0.6$  is assumed (Aharonian & Atoyan 1996; Strong et al. 2007), not specifying a concrete turbulence model for the whole range of the turbulent spectrum. Therefore, the data points in Fig. 3.10 and Fig. 3.11 are fitted with linear functions in the chosen double logarithmic representation. The points of the data sets  $D_{\perp}(E)$ , however, do not show a linear scaling over the entire explored energy range, but show a clear break which separates two regimes. Each of these regimes (the ranges right hand side and left hand side of the break) can be modeled assuming a linear scaling of the diffusion coefficient  $D_{\perp}(E)$  in a double logarithmic representation. Such a break in the energy dependence of diffusion coefficients has already been observed in the analysis of Fatuzzo et al. (2010). These authors analyzed the diffusion length as a function of energy for a constant point in time, meaning that they indirectly analyzed the diffusion coefficient as a function of energy. Following Fatuzzo et al. (2010), the quantity  $E_0$  is introduced, defined as

$$E_0 = \lambda_{\text{max}} e c B_0, \quad (3.20)$$

the energy of a particle with a gyroradius equal to the value of the maximum turbulent wavelength. For the chosen parameter values, this energy is  $E_0 = 4.62 \times 10^{16} (10^{17})$  eV for  $B_0 = 50$  (500)  $\mu\text{G}$ . A dimensionless parameter  $\epsilon = E/E_0$  can be defined, which helps

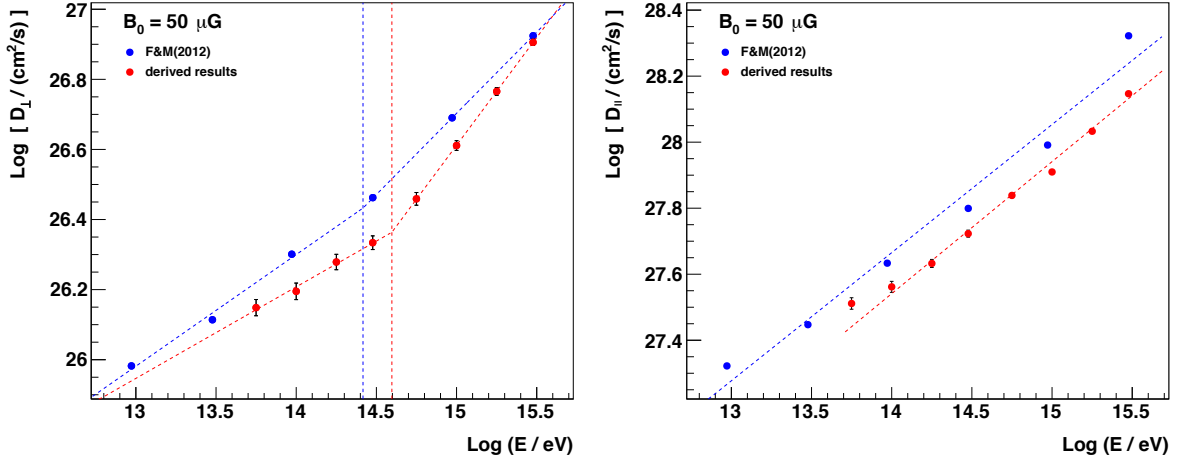


**Fig. 3.10:** Derived results for  $D_{\perp}(E)$  (left) and  $D_{\parallel}(E)$  (right) for a magnetic field strength of  $B_0 = 50 \mu\text{G}$ , shown as red points. The blue data points depict the results derived by Fatuzzo & Melia (2012). Dashed curves represent linear fit curves to the data points in the chosen double logarithmic representation. The data points of the quantity  $D_{\perp}(E)$  suggest a break in the slope of the fit curves, as indicated by vertical dashed lines. A detailed discussion is given in the text.

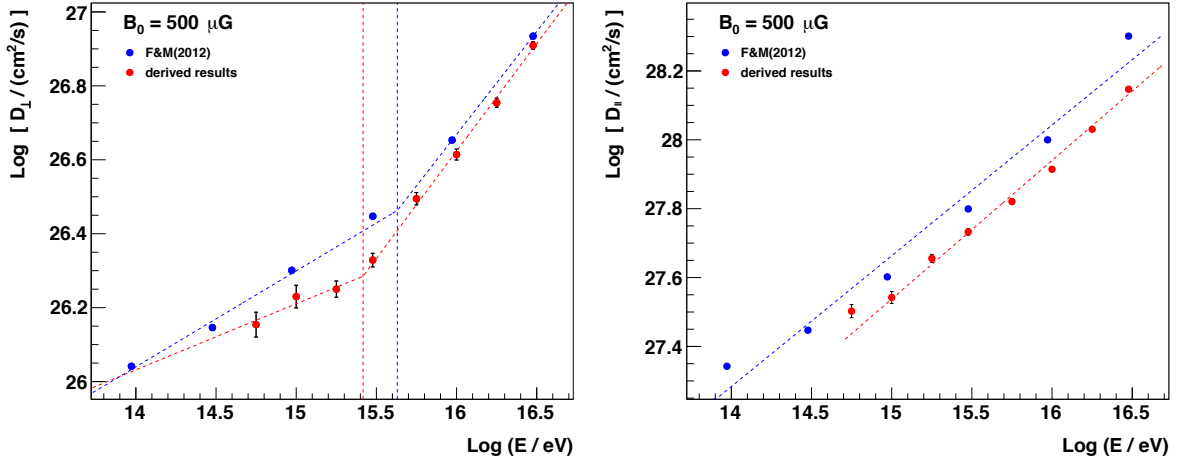


**Fig. 3.11:** Derived results for  $D_{\perp}(E)$  (left) and  $D_{\parallel}(E)$  (right) for a magnetic field strength of  $B_0 = 500 \mu\text{G}$ . The presentation is identical to the one in Fig. 3.10 showing the results for  $B_0 = 50 \mu\text{G}$ . Note the different scale of the energy axis.

to characterize the position of the described break in the linear scaling of  $\text{Log}(D_{\perp}(E))$  as a function of energy  $\text{Log}(E)$ . The exact analysis and the determination of the break is carried out as follows. A linear function is fitted to the data points below the value  $\text{Log}(E/\text{eV}) < 14.5$  ( $15.5$ ), and a second linear function is fitted to the data points above the value  $\text{Log}(E/\text{eV}) > 14.5$  ( $15.5$ ). The break is then calculated as the intersection point of these fitted functions. Note that the data point at energy  $\text{Log}(E/\text{eV}) \approx 14.5$  ( $15.5$ ) is not included in the fit procedure due to the uncertainty of the exact position of the

break. The described procedure is applied to the results of this analysis (red data points), and to the diffusion coefficients from the analysis of Fatuzzo & Melia (2012) (blue data points). The obtained values for the break,  $\epsilon_{\text{break}}$ , are summarized in Tab. 3.1. They show fluctuations in a range between  $0.006 \leq \epsilon_{\text{break}} \leq 0.009$ , in good agreement with the value of  $\epsilon_{\text{break}} \sim 0.01$ , given by Fatuzzo et al. (2010).

**Table 3.1:** Summary of the derived values for the break position  $\epsilon_{\text{break}}$  for the case of a turbulent magnetic field superimposed by a static background component.

	this work	Fatuzzo & Melia (2012)
$\epsilon_{\text{break}} (50 \mu\text{G})$	0.009	0.006
$\epsilon_{\text{break}} (500 \mu\text{G})$	0.006	0.009

The observation of the break might be interpreted as a change in the dynamics of particles, as particles with  $\epsilon \ll \epsilon_{\text{break}}$  are strongly coupled to the magnetic field lines and their diffusion is primarily dictated by the field structure and less by the value of their gyroradius. In contrast, particles with an energy  $\epsilon > \epsilon_{\text{break}}$  have a gyroradius large enough to decouple from the field lines and hence random walk through the field on length scales equal to their gyroradius. Thus, the dynamics of these particles is not particularly sensitive to the nature of the small-scale fluctuations and the output values essentially become independent of the exact value of  $\Gamma$  (Fatuzzo et al. 2010). Consequently, the argumentation on the influence of the choice of the value of  $\Gamma$  in Section 3.2.4 must be seen under the condition of working in this high-energy regime above the break, as the value of the maximum wavelength was set to  $\lambda_{\text{max}} = 10R_g$  there.

A break in the energy dependence of  $D_{\parallel}(E)$  is not visible, which is also in agreement with the results of Fatuzzo et al. (2010). The data points for  $D_{\parallel}(E)$  show clearly higher values than the ones for  $D_{\perp}(E)$ , reflecting the influence of the homogeneous background component.

In general, a change of the field strength from  $B_0 = 50 \mu\text{G}$  to  $B_0 = 500 \mu\text{G}$  means a change of a factor 10 for the gyroradius  $R_g$  of the particles. This change is compensated by a change in the energy of the particles by the same factor. Therefore, only scaling differences are to be expected concerning the dynamics of particles. Hence, the same values for diffusion coefficients should be obtained for both field strengths, with respect to a constant offset of one unit along the energy axis (in the chosen double logarithmic scale), in good agreement with the attained results. The values of the diffusion coefficients derived in this work are a little bit smaller for all shown cases than the ones given by Fatuzzo & Melia (2012). But it has to be noted that the analysis of the previously named authors additionally included the modeling of an electric field, which could explain the slightly different results. Moreover, the particle-tracking algorithm might differ from the one used in this work. However, differences are small and the development of the derived diffusion coefficients as a function of energy generally show good agreement.

The resulting fit parameters for the diffusion coefficients derived in this work are given in Tab. 3.2. The values for the index  $\delta$  of the assumed power-law dependence of the diffusion coefficient show fluctuations between  $\delta \sim 0.18 - 0.62$ , in agreement with the usually assumed values of  $\delta \sim 0.3 - 0.6$ . Compared to an expected value of  $\delta = 1/3$  for the specified case of Kolmogorov turbulence, the values derived for  $D_{\perp}(E)$ ,  $\epsilon \leq \epsilon_{\text{break}}$  are in agreement within the calculated errors, whereas the values for  $D_{\parallel}(E)$  tend to point to higher values. In the

regime above the break, values approximately twice as large as the value expected from standard theory are obtained. Turning to the absolute values obtained for the quantity  $D_{10}$ , the ones obtained for  $D_{\parallel}(E)$  are found slightly below the lower border of the usually quoted range for molecular cloud environments,  $D_{10} \sim 10^{26} - 10^{28} \text{ cm}^2/\text{s}$  (see e.g. Aharonian & Atoyan 1996; Gabici et al. 2009). The values obtained for  $D_{\perp}(E)$  are about one order of magnitude smaller than this range, however they are compatible with it regarding the calculated errors. Note that values of  $D_{10}$  for  $\epsilon > \epsilon_{\text{break}}$  are only given for consistent parametrization, but are not to be compared with this range.

**Table 3.2:** *Obtained fit parameters for the case of a turbulent magnetic field superimposed by a static component. The results refer to the red data points, derived in this work.*

Data set		$\text{Log}[ D_{10}/(\text{cm}^2/\text{s}) ]$	$\delta$
$D_{\perp}(E), B_0 = 50 \mu\text{G}$	$\epsilon \leq \epsilon_{\text{break}}$	$25.1 \pm 1.1$	$0.26 \pm 0.06$
	$\epsilon > \epsilon_{\text{break}}$	$23.5 \pm 0.4$	$0.62 \pm 0.02$
$D_{\perp}(E), B_0 = 500 \mu\text{G}$	$\epsilon \leq \epsilon_{\text{break}}$	$25.3 \pm 1.4$	$0.18 \pm 0.08$
	$\epsilon > \epsilon_{\text{break}}$	$23.1 \pm 0.5$	$0.58 \pm 0.03$
$D_{\parallel}(E), B_0 = 50 \mu\text{G}$		$25.9 \pm 0.1$	$0.40 \pm 0.01$
$D_{\parallel}(E), B_0 = 500 \mu\text{G}$		$25.5 \pm 0.1$	$0.40 \pm 0.01$

### Purely turbulent field

The derived results for the diffusion coefficient  $D(E)$  for the case of a purely turbulent field are shown in Fig. 3.12. As in the previous analysis of  $D_{\perp}(E)$ , the data exhibit a break, separating two different dynamical regimes as discussed above. Again, the derived diffusion coefficients are fitted with linear functions on a double logarithmic scale, above and below the break, respectively. The data point at  $\text{Log}(E/\text{eV}) \approx 14.5$  (15.5) for  $B_0 = 50 \mu\text{G}$  ( $500 \mu\text{G}$ ) is excluded from the fit procedure, just as in the analysis of  $D_{\perp}(E)$ , due to the uncertainty of the exact position of the break. A calculation of the break positions as the intersection points of the fit curves give values of  $\epsilon_{\text{break}} = 0.009$  ( $50 \mu\text{G}$ ) and  $\epsilon_{\text{break}} = 0.008$  ( $500 \mu\text{G}$ ), indicated in the figures as vertical lines. Fatuzzo et al. (2010) derived a value of  $\epsilon_{\text{break}} \sim 0.005$  for the case of a purely turbulent field, close to the here obtained values. The resulting fit parameters of the fitted functions are given in Tab. 3.3.

**Table 3.3:** *Obtained fit parameters for the case of a purely turbulent magnetic field.*

Data set		$\text{Log}[ D_{10}/(\text{cm}^2/\text{s}) ]$	$\delta$
$D(E), B_0 = 50 \mu\text{G}$	$\epsilon \leq \epsilon_{\text{break}}$	$24.9 \pm 1.2$	$0.42 \pm 0.07$
	$\epsilon > \epsilon_{\text{break}}$	$22.8 \pm 0.3$	$0.88 \pm 0.02$
$D(E), B_0 = 500 \mu\text{G}$	$\epsilon \leq \epsilon_{\text{break}}$	$24.6 \pm 1.2$	$0.40 \pm 0.06$
	$\epsilon > \epsilon_{\text{break}}$	$22.0 \pm 0.3$	$0.88 \pm 0.02$

The values obtained for the spectral index  $\delta$  for the case  $\epsilon \leq \epsilon_{\text{break}}$  are in agreement with the expected value for Kolmogorov turbulence of  $\delta = 1/3$  and are centrally positioned in the generally assumed range of  $\delta \sim 0.3 - 0.6$ . The values for the diffusion coefficient at an energy of 10 GeV,  $D_{10}$ , are about one order of magnitude smaller than the lower border of

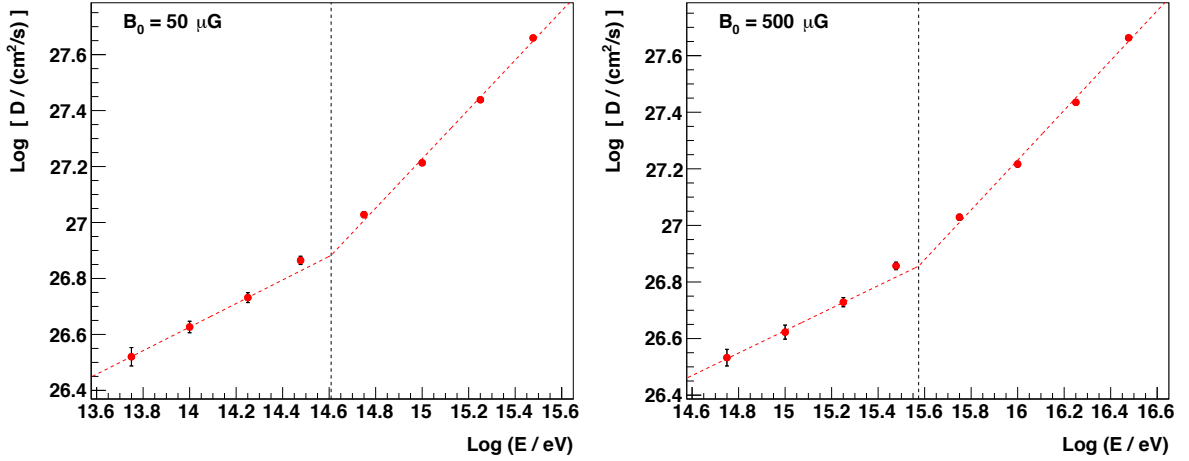


**Fig. 3.12:** Derived results for the diffusion coefficient  $D(E)$  for  $B_0 = 50 \mu\text{G}$  (left) and  $B_0 = 500 \mu\text{G}$  (right). As in the analysis of  $D_{\perp}(E)$ , the here shown data points exhibit a break in the assumed linear scaling of  $\text{Log}(D)$ , the diffusion coefficient, as a function of  $\text{Log}(E)$ , the energy. Dashed curves represent linear fit curves to the data points, the vertical dashed lines indicate the position of the break. Again, only a shift of a constant factor of 1 along the x axis is the only significant difference between the data points obtained for the different field strengths, as expected.

the usually assumed range for molecular cloud environments, being  $D_{10} \sim 10^{26} - 10^{28} \text{ cm}^2/\text{s}$ . However, regarding the uncertainties of the derived values, they are compatible with this range. Turning to the regime with energies  $\epsilon > \epsilon_{\text{break}}$ , the obtained values for  $\delta$  are  $\delta \sim 0.88$ , again showing a stronger dependence between the diffusion coefficient and the energy of particles than in the regime below the break.

In summary, the results derived in this analysis suggest that particle diffusion is to be separated in different dynamical regimes, as indicated by the observation of the break in the energy dependence of the diffusion coefficient for diffusion across the underlying magnetic field in case of a turbulent field superimposed by a static component, and for diffusion in a purely turbulent magnetic field. This is an important result for future analysis, as it shows that the usual assumption, in which the diffusion coefficient is assumed to follow a power law with a constant, energy independent spectral index  $\delta$ , might have to be reassessed. The derived results are generally in good agreement with the results of numerical analysis of other authors, especially the observation of the two different dynamical regimes for the applied formalism is consistent with the results of Fatuzzo et al. (2010). The obtained values for the spectral index  $\delta$  for the case  $\epsilon \leq \epsilon_{\text{break}}$  are compatible with the expected range. The obtained values for the parameter  $D_{10}$  tend to point to values about one order of magnitude smaller than the lower border of the usually quoted range of  $D_{10} \sim 10^{26} - 10^{28} \text{ cm}^2/\text{s}$ , but are compatible with these values within the estimated errors. As the exact magnetic field configuration in the Galactic Center is still not very well known (see discussion Chapter 3.3.1), only the derived diffusion coefficients for the case of a purely turbulent magnetic field will be used for a modeling of diffuse  $\gamma$ -ray emission in the Galactic Center region.

# 4 Modeling the diffuse $\gamma$ -ray emission from the Galactic Center region

As described in Section 2.2, one of the most promising scenarios which could explain the observed diffuse  $\gamma$ -ray emission from the Galactic Center region assumes that charged hadronic particles are accelerated by a central source and propagate out into the ambient space. The interactions of the diffusing particles with ambient matter, which can be modeled as proton-proton interactions (see Section 2.2), lead to the observable  $\gamma$ -ray excess. In this chapter, a modeling of the diffuse  $\gamma$ -ray emission from the inner Galactic Center region according to this scenario is presented. In the first part, the developed model is described in detail, including a discussion of long-distance particle tracking and the presentation of a density map of molecular clouds located at the Galactic Center region. Subsequently, the entire simulation procedure is summarized, including a discussion of principal physical assumptions and depicting the implementation of the interaction processes. In the second part of this chapter, this formalism is applied to diffusion coefficients at the upper end of the usually proposed range for diffusion processes in molecular clouds ( $D_{10} \sim 10^{28} \text{ cm}^2/\text{s}$ ) as well as to those derived in this work ( $D_{10} \sim 10^{25} \text{ cm}^2/\text{s}$ , see Section 3.3.2). The results of these simulations are presented and discussed.

## 4.1 The model

In this first section, the method used for a three-dimensional tracking of protons is introduced alongside a density map of molecular material, which represents the distribution of the molecular clouds in the Galactic Center region. A tracking according to the Lorentz force equation as presented for the derivation of diffusion coefficients (see Chapter 3) is computationally not feasible, given the small gyroradius of the particles compared to galactic distances. Instead, the diffusion equation is discretized using the finite difference method and protons are tracked on a discrete three-dimensional grid. Having introduced this framework, the entire simulation procedure will be summarized. Within this overview, important physical assumptions like the input proton spectrum as well as the implementation of interaction processes and the calculation of  $\gamma$ -ray fluxes are discussed.

### 4.1.1 Long-distance particle tracking

The tracking of the starting proton distribution, assumed to be released by a single impulsive ejection of the central source, is done via a discretization of the diffusion equation, here given again for completeness:

$$\frac{\partial n(E, \mathbf{r}, t)}{\partial t} = D(E) \nabla^2 n(E, \mathbf{r}, t) , \quad (4.1)$$

where  $n(E, \mathbf{r}, t)$  was defined as the number density of particles. Using the finite difference method, the individual terms of Eq. 4.1 can be rewritten in a discrete form as follows:

$$\frac{\partial n(x_i, y_j, z_k; t_m)}{\partial t} \approx \frac{n(x_i, y_j, z_k; t_{m+1}) - n(x_i, y_j, z_k; t_m)}{\Delta t} , \quad (4.2)$$

$$\frac{\partial^2 n(x_i, y_j, z_k; t_m)}{\partial x^2} \approx \frac{n(x_{i+1}, y_j, z_k; t_m) - 2n(x_i, y_j, z_k; t_m) + n(x_{i-1}, y_j, z_k; t_m)}{(\Delta x)^2} . \quad (4.3)$$

Here, equally spaced points along the spatial axes and the time axis are used to set up a discrete grid for working:

$$\begin{aligned} t_m &= t_0 + m \Delta t , & m &= 0, 1, \dots, M \\ x_i &= x_0 + i \Delta x , & i &= 0, 1, \dots, I \\ &\vdots & & \end{aligned} \quad (4.4)$$

A discretization of the space derivatives in y or z direction is carried out straightforward, analogously to the one in x direction (Eq. 4.3). The applied scheme is called Forward Time Central Space (FTCS) method, as the first-order forward difference is used to approximate the time derivative term and the second-order central difference is used to approximate the space derivatives. An introduction to finite differences and the discretization of differential equations can e.g. be found in Press et al. (1986). For a simplification of notation, let  $n_{i,j,k}^m$  denote  $n(x_i, y_j, z_k; t_m)$ . Then, the discretized equation is given as

$$\begin{aligned} \frac{n_{i,j,k}^{m+1} - n_{i,j,k}^m}{\Delta t} &= D \left( \frac{n_{i+1,j,k}^m - 2n_{i,j,k}^m + n_{i-1,j,k}^m}{(\Delta x)^2} + \frac{n_{i,j+1,k}^m - 2n_{i,j,k}^m + n_{i,j-1,k}^m}{(\Delta y)^2} \right. \\ &\quad \left. + \frac{n_{i,j,k+1}^m - 2n_{i,j,k}^m + n_{i,j,k-1}^m}{(\Delta z)^2} \right) . \end{aligned} \quad (4.5)$$

For this work, the distances of grid nodes are chosen equally in the three spatial directions, setting the denominators of the right-hand side to the same value, which will be denoted as  $(\Delta x)^2$ . Finally, solving Eq. 4.5 for  $n_{i,j,k}^{m+1}$  gives

$$\begin{aligned} n_{i,j,k}^{m+1} &= n_{i,j,k}^m (1 - 3c) + \frac{c}{2} \left( n_{i+1,j,k}^m + n_{i-1,j,k}^m + n_{i,j+1,k}^m + n_{i,j-1,k}^m \right. \\ &\quad \left. + n_{i,j,k+1}^m + n_{i,j,k-1}^m \right) , \end{aligned} \quad (4.6)$$

where  $c$  is defined as  $c = \frac{2D\Delta t}{(\Delta x)^2}$ . Thus, the number of particles for each grid node at the time  $t_{m+1}$  can be calculated from the known values of its direct neighbors and its own value at the preceding point in time,  $t_m$ . For the simulation, a three-dimensional space is set up by defining a three dimensional histogram with equal binning in all three spatial directions. The discrete nodes of the computing grid can be associated with the bin centers, and the number density of particles, which changes into a discrete number of particles for the discrete treatment, can be obtained by dividing it by the bin size. Equation 4.6 can be interpreted as follows: for each time step, a fraction of  $3c$  of the particles of a bin leaves and is replaced by a fraction of  $c/2$  from each of its direct neighbors. From a physical point of view, it is not possible that more particles leave a bin than it contained before, leading to the condition

$$3c = 3 \frac{2D\Delta t}{(\Delta x)^2} \leq 1 , \quad (4.7)$$

which is identical to the von Neumann stability criterion of the used method. The condition given in Eq. 4.7 restricts the maximum value of the adopted time step according to the applied diffusion coefficient  $D$  and the chosen bin size. After this short introduction of the tracking algorithm for the protons, the density map, which is embedded within the discrete three-dimensional histogram setting up the working environment, will be introduced in the following section.

### 4.1.2 Density map of molecular clouds

A density map depicting the distribution of the molecular material located in the Galactic Center region in form of dense molecular clouds is usually extracted from analysis of line emission of density-sensitive molecular species (see Section 3.3.1). The general problem for a three-dimensional modeling of such a density distribution is an adequate positioning of the material along the line-of-sight axis. A method to derive the positions of molecular clouds along the line-of-sight direction is presented in (Sawada et al. 2004). These authors used measurements of 2.6-mm CO emission lines and compared them with 18-cm OH absorption lines to derive a face-on velocity map that connects the line-of-sight position with a certain velocity value. Consequently, such a face-on velocity map can be used as look-up table to achieve a positioning of molecular material along the line of sight. A suitable data set depicting the density distribution of the Galactic Center molecular clouds is provided by the extended CS(1-0) mapping of the Galactic Center region with the 45 m telescope at Nobeyama Radio Observatory (Tsuboi et al. 1999). The data set provides maps of CS emission in the velocity range from  $v = -200$  km/s to  $v = 200$  km/s, integrated in velocity bands of a width of  $\Delta v = 10$  km/s. The extension of the whole mapping region is from about  $-1.1^\circ$  to  $1.7^\circ$  in Galactic longitude and  $-0.3^\circ$  to  $0.2^\circ$  in Galactic latitude, see Fig. 4.1. A three-dimensional density map for the Galactic Center region based on the named CS-data set was set up by Nekrassov (2010). There, the information provided by Sawada et al. (2004) was used for an adequate positioning of the molecular material along the line of sight, as described above. For a detailed description of the three-dimensional map modeling see Nekrassov (2010). The density map designed by Nekrassov (2010) was used as a basis for setting up a three-dimensional cloud distribution of the Galactic Center region in this work. The original map was re-binned to match the desired configurations of the discrete computing grid. To allow quantitative calculations, the density values assigned to the individual bins were furthermore converted in such a way that the cloud density is on average  $\langle n_H \rangle = 2\langle n_{H_2} \rangle = 10^4$  cm $^{-3}$ , following the estimated values for cloud densities of the Galactic Center region, see Section 3.3.1.

### Working environment

The three-dimensional histogram used as working environment in this work is designed equally spaced along all three spatial directions. 105 bins with a constant width of 10 pc set up each spatial axis. The Galactic Center is defined as the central bin. Thus, the environmental area considered by the calculation grid comprises a distance of about 525 pc from the Galactic Center in each direction. A conversion from pc to degrees can be done using the relation  $1^\circ \approx 148$  pc for an assumed distance of the Galactic Center of 8.5 kpc. Hence, the bin width is  $\sim 0.07^\circ$  and the covered area comprises more than  $\pm 3^\circ$  in each spatial direction. The density distribution of molecular clouds used to simulate the diffuse  $\gamma$ -ray emission is adjusted to these settings.

In Fig. 4.2, this distribution is shown as a projection onto the plane perpendicular to the

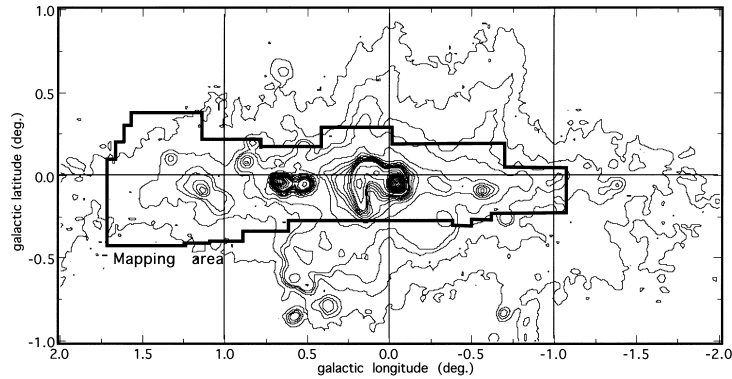


**Fig. 4.1:** Observation area of the CS(1-0) mapping of the molecular cloud distribution in the Galactic Center region carried out by Tsuboi et al. (1999). The thick black line depicts the contour line of the mapping region. The picture is taken from Tsuboi et al. (1999).

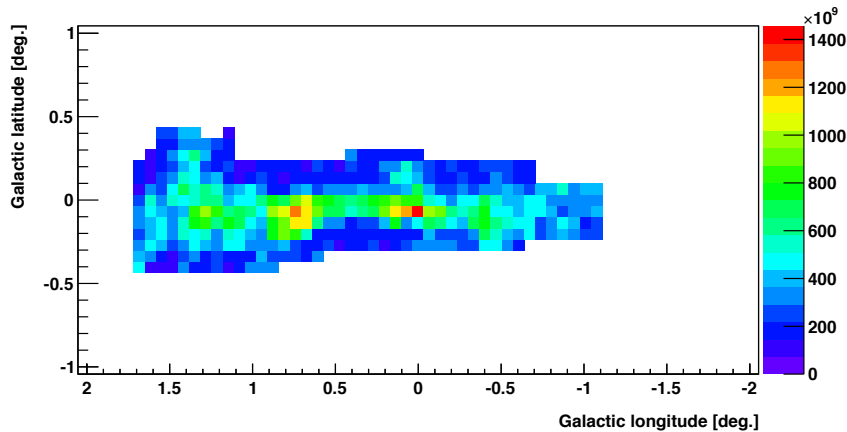


**Fig. 4.2:** Constructed density map of molecular clouds in the Galactic Center region as a projection perpendicular to the line-of-sight axis. As a basis for this map, the map set up in (Nekrassov 2010) was used, which is build up upon the CS observations of Tsuboi et al. (1999), see Fig. 4.1. Small deviations of the contour of the filled area from the one used for the CS-mapping arise from the binning adjustment. The color scale of the figure represents the integrated density along the line of sight, in units of  $\text{m}^{-3}$ .

line-of-sight axis. The contour of the filled area corresponds to the one of the area covered by the CS(1-0) observation of the Galactic Center region by Tsuboi et al. (1999) shown in Fig. 4.1. Small deviations are visible due to the binning-adjustment. A projection of the density distribution onto the plane showing the line-of-sight axis vs. Galactic longitude is illustrated in Fig. 4.3. This figure shows that more material is shifted towards positive direction along the line of sight than in negative direction.

Having set up the environmental framework of the model in the last two sections, the next section gives an overview of the entire simulation procedure and depicts how the interactions of protons with the surrounding matter are implemented.

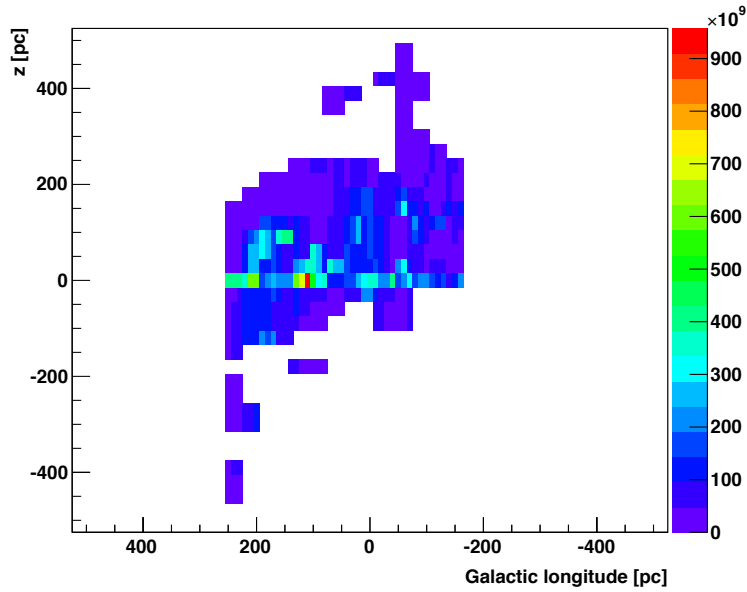


**Fig. 4.3:** Constructed density map of molecular clouds in the Galactic Center region, integrated over Galactic latitude. The line-of-sight axis is depicted as  $z$  axis. The color scale is given in  $\text{m}^{-3}$ . The shown positioning of the molecular material along the line-of-sight axis is reached using a face-on velocity distribution of the region, provided by Sawada et al. (2004).

#### 4.1.3 Simulation procedure and interaction processes

For modeling the diffuse  $\gamma$ -ray emission in the Galactic Center region, it is assumed that the diffusing protons are released by a single impulsive ejection of the source, which is located in the central bin of the working environment, i.e. at the origin of the Galactic coordinate system. The differential energy spectrum of the protons is assumed to follow a power law:

$$\frac{dN_p(E_p)}{dE_p} \propto E_p^{-2} . \quad (4.8)$$

Here,  $E_p$  denotes the energy of the protons and  $dN(E_p)$  the number of protons in the energy interval  $(E_p, E_p + dE_p)$ . The amount of energy to be spent into acceleration of charged particles for the hadronic diffusion scenario is estimated to be  $\sim 10^{50}$  erg for an energy range that extends from  $10^9 - 10^{15}$  eV, see Aharonian et al. (2006a). The energy range considered here for a simulation of the diffuse  $\gamma$ -ray emission extends from  $10^{11} - 10^{17}$  eV. The total number of particles for this interval is, thus, calculated to meet the estimate given by Aharonian et al. (2006a). For numerical computation, the energy spectrum for the considered range  $-1 \leq \text{Log}(E_p/\text{TeV}) \leq 5$  is set up using 300 bins equally spaced on a logarithmic scale. For each energy bin, the particles are released in the central spatial bin of the three-dimensional histogram setting up the tracking environment at the time  $t = 0$ . The particles are tracked on the discrete computation grid in discrete time steps  $\Delta t$  as described in Section 4.1.1. At each time step, a number of protons  $N_{\text{loss},ijk}$  will be lost in each spatial bin  $(i, j, k)$  due to interactions with the ambient material. This

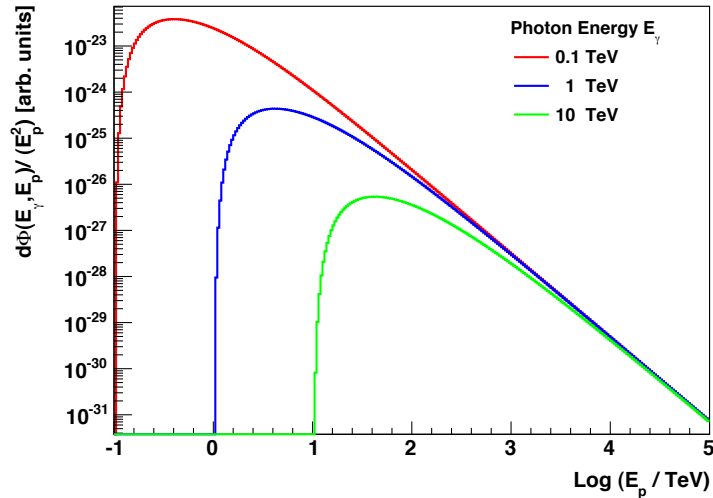


**Fig. 4.4:** Flux  $d\Phi(E_\gamma, E_p)$  as a function of the proton energy  $E_p$  for three different photon energies  $E_\gamma$ . The flux is weighted with  $E_p^{-2}$ , the scaling of the input energy spectrum of the protons (see Eq. 4.8). By the shown weighting, it is visible that photons of energy  $E_\gamma$  are mainly created by protons of energy  $E_p \approx 4E_\gamma$ , as the shown curves reach their maximum value at this position, respectively.

number is calculated via the formula

$$\frac{N_{loss,ijk}}{N_{ijk}} = 1 - \exp(-n_{ijk}\sigma v\Delta t) \quad . \quad (4.9)$$

Note that here,  $n_{ijk}$  denotes the density of the ambient material of the bin  $(i, j, k)$ , and  $N_{ijk}$  denotes the number of protons in it.  $v \approx c$  denotes the velocity of the particles and  $\sigma$  is the proton-proton cross-section. The parametrization given in (Kelner et al. 2006) is used for its calculation. Having reached the total desired tracking time, the  $\gamma$ -ray spectrum resulting from each spatial bin  $(i, j, k)$  due to proton-proton interactions is calculated using the results given in (Kelner et al. 2006). These authors give analytical parametrizations of the energy spectra of secondary particles like  $\gamma$ -rays, produced in inelastic proton-proton interactions for energies  $E_p > 100$  GeV. A two-dimensional look-up table giving the resulting flux  $d\Phi(E_\gamma, E_p)$  in discrete energy bins, can be build up upon these results. It is shown as a function of  $E_p$  in Fig. 4.4 for three different photon energies  $E_\gamma$ . In (Nekrassov 2010), a very similar plot is shown, allowing a cross-check for the calculations carried out. For the  $\gamma$ -ray spectrum, the same energy range and same binning as for the proton spectrum is used, i.e. 300 bins equally spaced on a logarithmic scale  $-1 \leq \text{Log}(E_\gamma/\text{TeV}) \leq 5$ . The look-up table is set up as two-dimensional histogram in such a way that the  $\gamma$ -ray flux for a given spatial bin is simply obtained by a multiplication of the entries of the look-up table with the number of protons (at considered energy) contained in the spatial bin and with its density value. The complete  $\gamma$ -ray spectrum produced by the protons of the entire considered energy range is obtained by a summation over the  $\gamma$ -ray spectra resulting from the individual energy bins of the proton spectrum.

For a calculation of the  $\gamma$ -ray flux measured on earth, it is assumed that the radiation of each bin is emitted isotropically in  $4\pi$  steradians. The results of the simulation will be

compared to those obtained from the analysis of the diffuse  $\gamma$ -ray emission at the Galactic Center region with the H.E.S.S. instrument, see Aharonian et al. (2006a). Therefore,  $\gamma$ -ray count maps are calculated with the simulation in addition to the  $\gamma$ -ray flux spectrum, as they allow a comparison of the morphology of the  $\gamma$ -ray emission. For this purpose, an observation time of 55 hours is used (see Aharonian et al. 2006a). Furthermore, the effective area for the H.E.S.S. instrument given in (Aharonian et al. 2006c) is adopted for all calculations, to allow a comparison of results. In the following sections, different values of the diffusion coefficient  $D(E)$  will be applied to the introduced formalism for a modeling of the diffuse  $\gamma$ -ray emission from the Galactic Center region.

## 4.2 Results of the modeling and comparison to the H.E.S.S. data

In the developed formalism for a simulation of the diffuse  $\gamma$ -ray emission from the Galactic Center region, the diffusion coefficient  $D(E)$  enters as free input parameter. Within this section, a first run of the simulation is performed choosing  $D_{10} = 10^{28} \text{ cm}^2/\text{s} \approx 0.03 \text{ pc}^2/\text{yr}$ . This value refers to the upper end of the usually assumed range for cosmic ray diffusion in molecular clouds, and is about three orders of magnitude larger than the ones derived in this work (see Section 3.3.2). Afterwards, the diffusion coefficients derived in this work are applied to the formalism. The obtained results of these simulations are discussed and compared to the H.E.S.S. data from the analysis of Aharonian et al. (2006a).

### 4.2.1 Results for commonly proposed diffusion coefficients

For the setting  $D_{10} = 0.03 \text{ pc}^2/\text{yr}$ , it is assumed that the energy dependence of the diffusion coefficient can be described by a power law with constant index  $\delta$  over the entire considered energy range (see Eq. 3.19). The spectral index is varied within a range of  $\delta = 0.0 - 0.5$  ( $\Delta\delta = 0.1$ ). The total tracking time is set to  $10^4$  years. A discussion of the energy spectra and the spatial distributions of the protons after this time period will be given before the discussion of the  $\gamma$ -ray emission, which results from these distributions.

#### Proton spectra

The injection spectrum of the protons, injected in the central bin of the working environment at time  $t = 0$ , is shown in Fig. 4.5 on the left. The quantity  $N(E_p)$  gives the number of protons at energy  $E_p$ , i.e. the number of protons integrated over the corresponding energy bin. Therefore, the slope accounts  $-1$  in the shown double logarithmic representation, as  $dN_p/dE_p \propto E_p^{-2}$  was defined as start distribution for all simulations.

The proton spectra summed up over the entire working environment after a tracking time of  $10^4$  years are shown on the right hand side for the different spectral indices  $\delta$ . There are two interesting features visible. First, the spectra for  $\delta = 0.4/0.5$  quickly drop towards the upper end of the considered energy range. This is the result of high-energy diffusion, meaning that for high values of  $\delta$ , diffusion coefficients at high energies are so large that protons simply diffuse out of the considered volume. Secondly, there is a loss of particles over the entire energy range compared to the initial input spectrum. The extent of these particle losses, which originate from interaction processes during propagation, decreases with increasing value of  $\delta$ . This feature is again related to the velocity of the diffusion

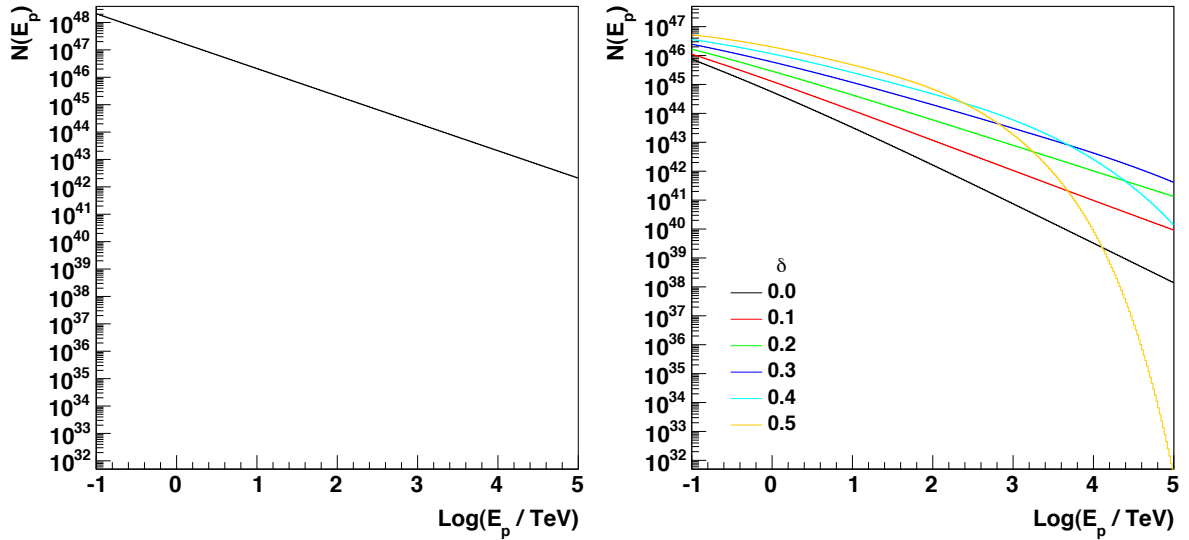


**Fig. 4.5:** Start proton spectrum at time  $t = 0$  (left) and proton spectra after a tracking time of  $t = 10^4$  years for  $D_{10} = 0.03 \text{ pc}^2/\text{yr}$  and various spectral indices  $\delta$ . The quantity  $N(E_p)$  gives the number of particles at energy  $E_p$ , i.e. the number of particles integrated over the corresponding energy bin. For higher values of  $\delta$  ( $\delta = 0.4/0.5$ ), the spectra quickly drop towards the upper end of the considered energy range, indicating that particles at high energies diffuse so fast for the higher  $\delta$ -values that they leave the working environment.

process, as larger values of  $\delta$  mean that the protons diffuse faster out of the central, dense region and therefore, the losses due to particle interactions are smaller compared to those at lower values of  $\delta$ . The effect is more pronounced for higher energies than for smaller ones, as a change in the spectral index of the power law  $D(E) \propto E^\delta$  results in a stronger increase in the output values  $D$  for the higher energies in the considered energy range than for smaller ones. This is clearly visible in Fig. 4.5, as the differences of the spectra for the various spectral indices  $\delta$  are more pronounced towards higher energies. For energy independent diffusion, shown by the black curve ( $\delta = 0.0$ ), the influence of the energy dependence of the proton-proton cross-section becomes visible, as this quantity makes the only difference in the tracking processes of the proton distributions in different energy bins for  $\delta = 0.0$ . Due to its increasing values with increasing energy, the spectrum slightly steepens towards higher energies.

To gain a deeper insight into the spatial distributions of the protons, Fig. 4.6 shows the distributions of the particles along Galactic longitude as a function of particle energy  $E_p$  for the six different considered values of  $\delta$ . The form of the distributions along Galactic longitude can be described by single Gaussian distributions of different widths for different energy values, respectively. In all cases, the influence of the power-law scaling of the energy spectrum is clearly visible, as for constant values of Galactic longitude, the bin contents decrease towards higher energies. For the case  $\delta = 0.0$ , the width of the distributions therefore seems to decrease. This effect is more and more compensated for higher values of  $\delta$ , as the width of the distributions increases for  $\delta \neq 0$ . The extent of this increase is, as already mentioned, more pronounced for higher energies than for the smaller ones in the considered energy range. For the highest values of  $\delta$  ( $\delta = 0.4/0.5$ ), the width of the distributions has

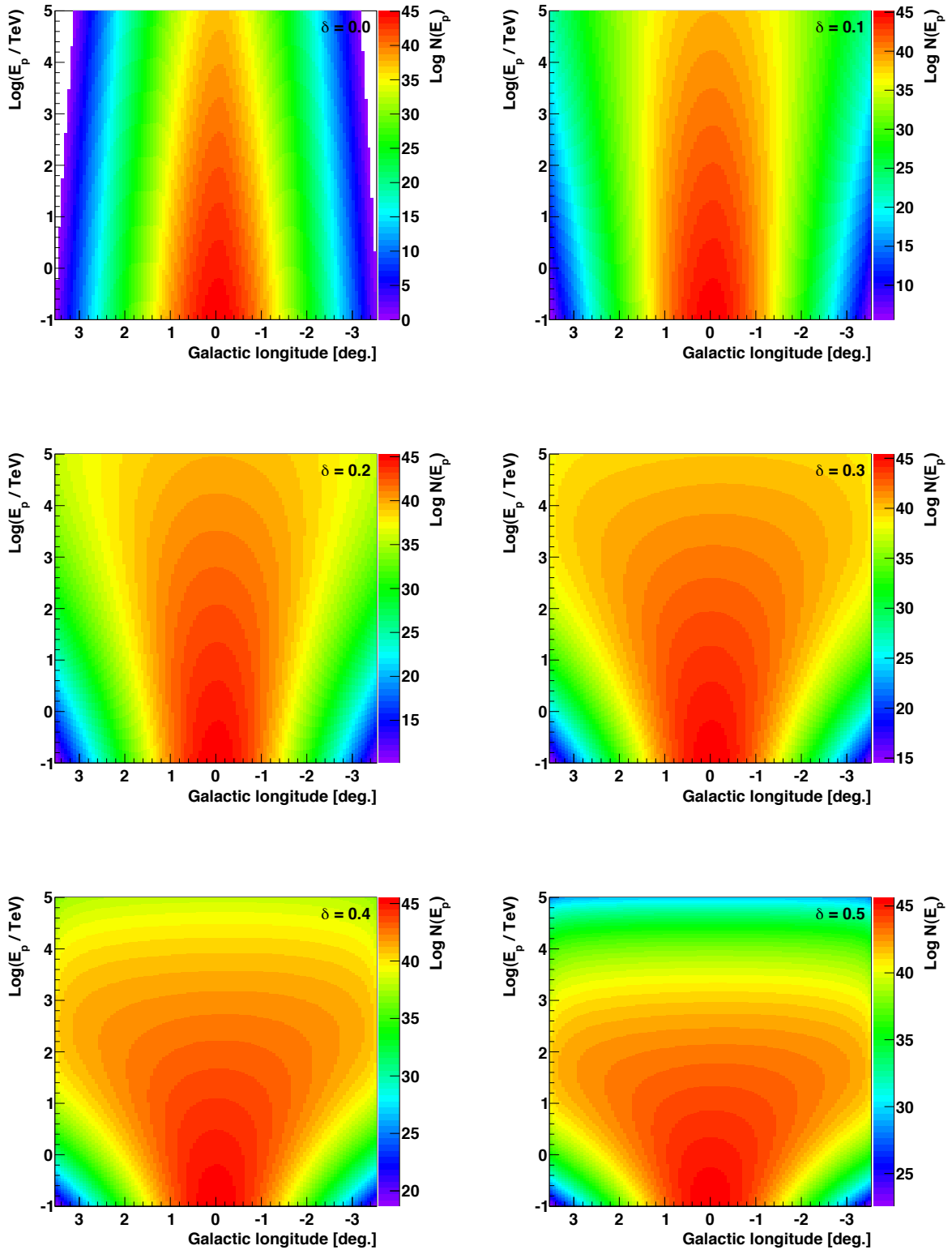


**Fig. 4.6:** Proton spectra  $N(E_p)$  along Galactic longitude after a total tracking time of  $10^4$  years ( $D_{10} = 0.03 \text{ pc}^2/\text{yr}$ ). The influence of the spectral index  $\delta$  of the power law dependence of the diffusion coefficient  $D(E)$  is clearly identifiable, as with increasing values of  $\delta$ , the width of the distributions along Galactic longitude increases. This effect is more pronounced towards higher energies.

grown up to such values at high energies that after the tracking time of  $10^4$  years, the values of the distributions for constant energy show no significant variation over the entire range in Galactic longitude. This indicates that a non-negligible fraction of protons has diffused out of the considered volume. This outcome is, as already discussed, also clearly visible in Fig. 4.5, as the spectra for  $\delta = 0.4/0.5$  drop quickly towards the upper end of the considered energy range. As expected and highlighted in the discussion, the spectral index  $\delta$  has strong influence on the development of the protons' spatial distribution and will therefore have influence on the observable  $\gamma$ -ray emission, which will be discussed next.

#### $\gamma$ -ray spectra and excess count maps

The  $\gamma$ -ray spectra at  $t = 10^4$  years, arising from interactions of the presented proton distributions with the ambient material, are shown in Fig. 4.7. To allow comparison with the H.E.S.S. measurement (blue dots), the analyzed region is restricted to  $|l| < 0.8^\circ$  and  $|b| < 0.3^\circ$ . Black curves depict the calculated flux as described in the previous sections without any corrections. The red curves depict a fit of these primary output spectra to the flux measured with the H.E.S.S. instrument. The fit procedure is set up using the  $\chi^2$  method as follows. A  $\chi^2$  value is defined, with the only free parameter being a normalization factor to match the measured data by the output of the simulation (black curve). Thus, the functional form of the primary output spectrum is not changed by the fit:

$$\chi^2 = \sum_{i=1}^9 \frac{(f_{H,i} - \alpha f_{S,i})^2}{\sigma_i^2} . \quad (4.10)$$

The  $\chi^2$  value is minimized, using symmetrized errors  $\sigma_i$  of the H.E.S.S. data points  $f_{H,i}$ . The flux calculated by the simulation at the corresponding energy is denoted by  $f_{S,i}$ . Hence, given 9 data points and the normalization factor  $\alpha$  which is to be optimized, the fit has 8 degrees of freedom (d.o.f.). The resulting values are summarized in Tab. 4.1.

To characterize the obtained  $\gamma$ -ray spectra, an additional fit assuming a power law dependence of the flux as a function of energy is performed to the curves in the energy range  $-1 < (E/\text{TeV}) < 1.3$ . Even though energy-dependent influences, which are already clearly visible in the shown proton spectra, imply that a simple power-law scaling is not sufficient to exactly describe the characteristic of the obtained spectra, this parametrization is assumed to obtain an analytical description. The resulting spectral indices  $\Gamma_\gamma$  are also given in Tab. 4.1.

**Table 4.1:** Fit parameters of the  $\chi^2$ -fit, as introduced in Eq. 4.10. The spectral indices  $\Gamma_\gamma$  are obtained from separate power-law fits to the spectra calculated with the simulation, assuming that these can be described by a simple power law in the energy regime  $-1 < (E/\text{TeV}) < 1.3$ .

$\delta$	$\alpha$	$\chi^2/\text{d.o.f.}$	p-value	$\Gamma_\gamma$
0.0	5.72	0.53	0.84	2.3
0.1	1.91	1.86	0.06	2.1
0.2	0.63	3.88	$1 \times 10^{-4}$	1.9
0.3	0.33	3.97	$1 \times 10^{-4}$	1.9
0.4	0.27	2.67	$6 \times 10^{-3}$	1.9
0.5	0.32	0.95	0.47	2.1

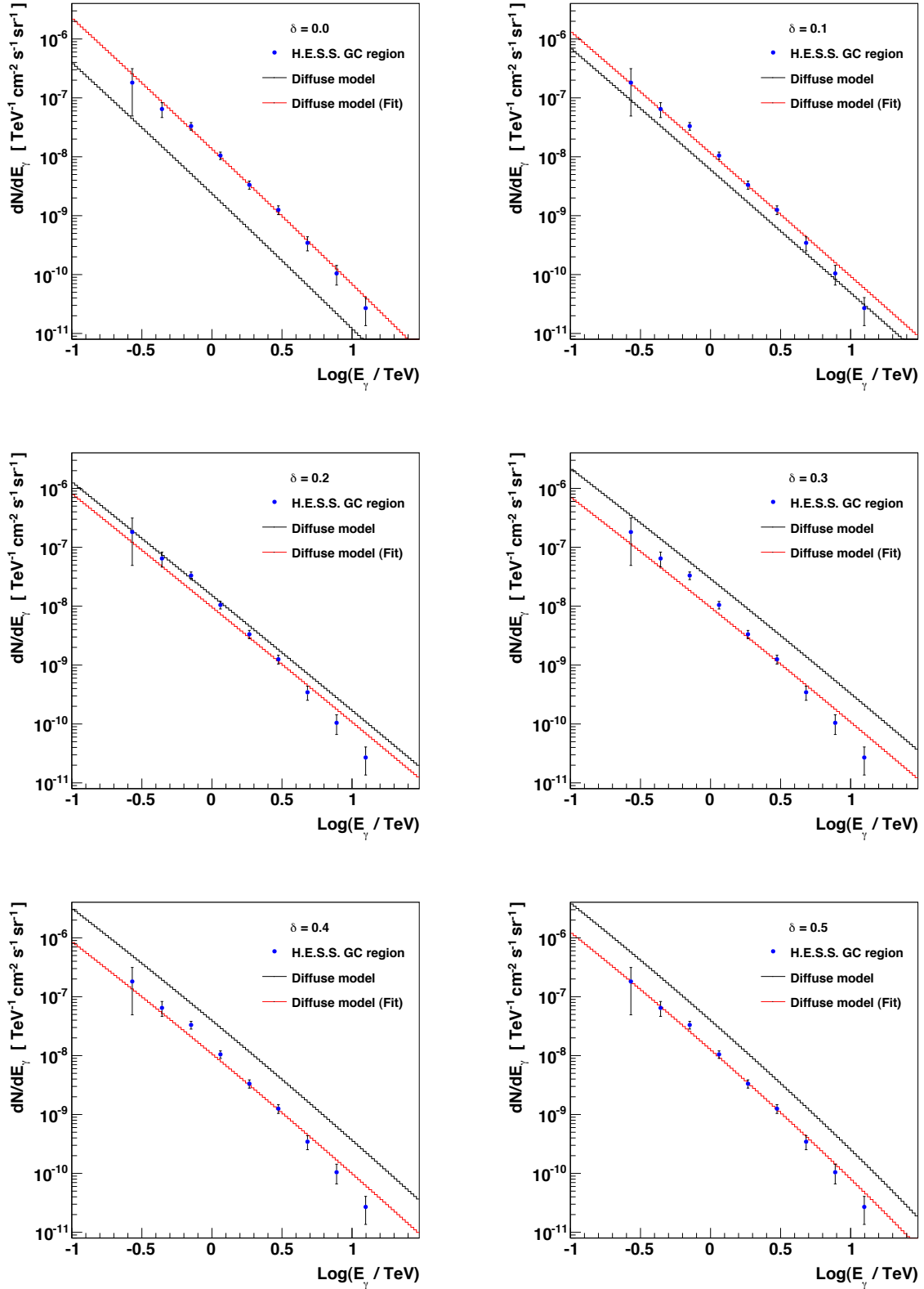


**Fig. 4.7:**  $\gamma$ -ray flux in the Galactic Center region obtained from the simulation for  $D_{10} = 0.03 \text{ pc}^2/\text{yr}$  and various values of  $\delta$ . The shown spectra refer to a region  $|l| < 0.8^\circ$  and  $|b| < 0.3^\circ$  to allow comparison to H.E.S.S. data (Aharonian et al. 2006a), shown using blue dots. Black curves correspond to uncorrected spectra directly obtained from the simulation, whereas red curves depict fit curves of this primary output spectra to the flux measured with the H.E.S.S. instrument.

In general, one can clearly observe the connection of the  $\gamma$ -ray spectra to the proton spectra they arise from, as with an increasing value of  $\delta$ , the entire uncorrected  $\gamma$ -ray spectra (black histograms, Fig. 4.7) are again shifted towards higher absolute values due to less losses of protons during the entire propagation period (see discussion above).

A striking outcome of the simulation is the fact that the calculated  $\gamma$ -ray spectra are to be found at the same order of magnitude as the flux measured by H.E.S.S. The normalization factors  $\alpha$  derived from the  $\chi^2$ -fit lie within a range of 0.27 – 5.72. As the total number of particles was set according to the estimate given by Aharonian et al. (2006a), to  $10^{50}$  erg for the range  $10^9 - 10^{15}$  TeV, the obtained values give a correction of this value to match the measured data as well as possible according to the defined  $\chi^2$  optimization. Therefore, the source energies obtained from the fit lie within a range of  $0.32 \times 10^{51}$  erg –  $5.72 \times 10^{51}$  erg, assuming 10% efficiency for particle acceleration. Hence, apart from the value for  $\delta = 0.0$ ,  $\alpha = 5.72$ , all derived energy values are realistic values to be delivered, for example, by a single supernova explosion with a typical explosion energy of  $10^{51}$  erg.

The resulting reduced  $\chi^2$  values lie within a range of 0.53 – 3.97 (d.o.f.=8). The corresponding calculated p-values show that for  $\delta = 0.2 - 0.4$ , only poor fits are obtained. The assumption that the data can be described by the simulation model can be rejected at a level of  $\sim 3.8\sigma$  for  $\delta = 0.2/0.3$  and  $\sim 2.5\sigma$  for  $\delta = 0.4$ . However, this statement only holds assuming that the errors of the data points follow a normal distribution. Nonetheless, for the values  $\delta = 0.2 - 0.4$ , the slope of the spectra obtained by the simulation appears not to fit quite well to the one of the data points. A better description is obtained for the values  $\delta = 0.0/0.1$  and  $\delta = 0.5$ , while the first two values can be rejected with regard to the morphology of the obtained excess region. This aspect will be discussed below during the presentation of the calculated excess count maps. For  $\delta = 0.5$ , the fit achieves  $\chi^2/\text{d.o.f.} = 0.95$ .

The spectral indices  $\Gamma_\gamma$ , obtained from power-law fits to the simulated spectra, slightly decrease from  $\delta = 0.0$  to  $\delta = 0.2$ , meaning that the spectra become flatter as the value of the spectral index decreases. Such a behavior already occurs in the spectra of the protons if one would assume that the lower end of the energy interval can be modeled by a power law, see Fig. 4.5. This effect can be understood as an interplay of the energy-dependent influences described above, the diffusion speed and the proton-proton interaction cross-section, and has already been indirectly discussed. Increasing values of the cross-section towards higher energies, leading to a steepening of the spectra towards higher energies, are more and more compensated by faster diffusion of the particles out of the central dense region with higher values of  $\delta$ . For  $\delta = 0.2$  to  $\delta = 0.4$ , this effect remains visible for the proton spectra shown in Fig. 4.5. The fitted indices of the  $\gamma$ -ray spectra, however, remain constant here. This difference is obviously connected to the restricted analysis area  $|l| < 0.8^\circ$  and  $|b| < 0.3^\circ$  for the  $\gamma$ -ray spectra. Finally, for  $\delta = 0.5$ , one observes the same effect for the proton and the  $\gamma$ -ray spectrum. Due to the fact that a significant fraction of the particles has diffused out of the considered volume, the spectra start to steepen again.

The next step is a discussion of the  $\gamma$ -ray excess count maps obtained from the simulation. In Fig. 4.8 and Fig. 4.9, the  $\gamma$ -ray excess calculated with the simulation is shown as longitude profile for the different considered values of  $\delta$  (green histograms). The normalization factors  $\alpha$ , which are obtained from the above described  $\chi^2$ -fit to match the flux measurement of the H.E.S.S. instrument, are thereby taken into account.

The black histogram shows the background-subtracted and acceptance-corrected excess counts of the diffuse emission from the Galactic Center region, measured with the H.E.S.S.

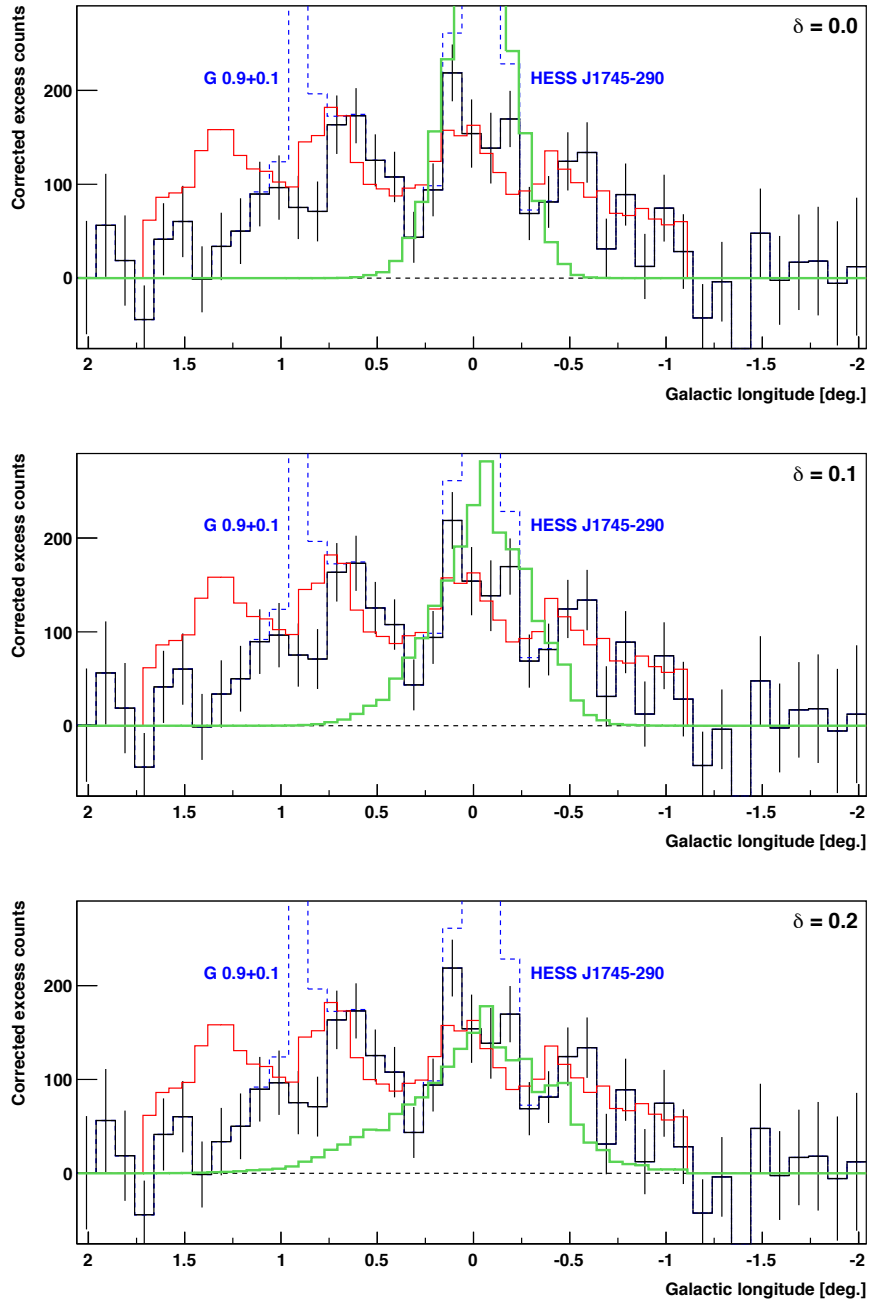


**Fig. 4.8:** Longitude profiles of  $\gamma$ -ray excess counts for  $|b| < 0.2^\circ$ , obtained from the simulation (green histogram) for  $D_{10} = 0.03 \text{ pc}^2/\text{yr}$  and different values of  $\delta$ . The black histogram shows the acceptance-corrected  $\gamma$ -ray counts measured with the H.E.S.S. instrument (data are taken from Aharonian et al. 2006a). The red curve depicts the density distribution of molecular gas. The energy threshold of the counts is 380 GeV.

instrument. The red curve depicts the density distribution of the molecular gas in the Galactic Center region, i.e. a projection of Fig. 4.2. It is clearly visible that with increasing value of  $\delta$ , the calculated excess region broadens along Galactic longitude, obviously connected with the increase in the width of the respective proton distributions, as discussed

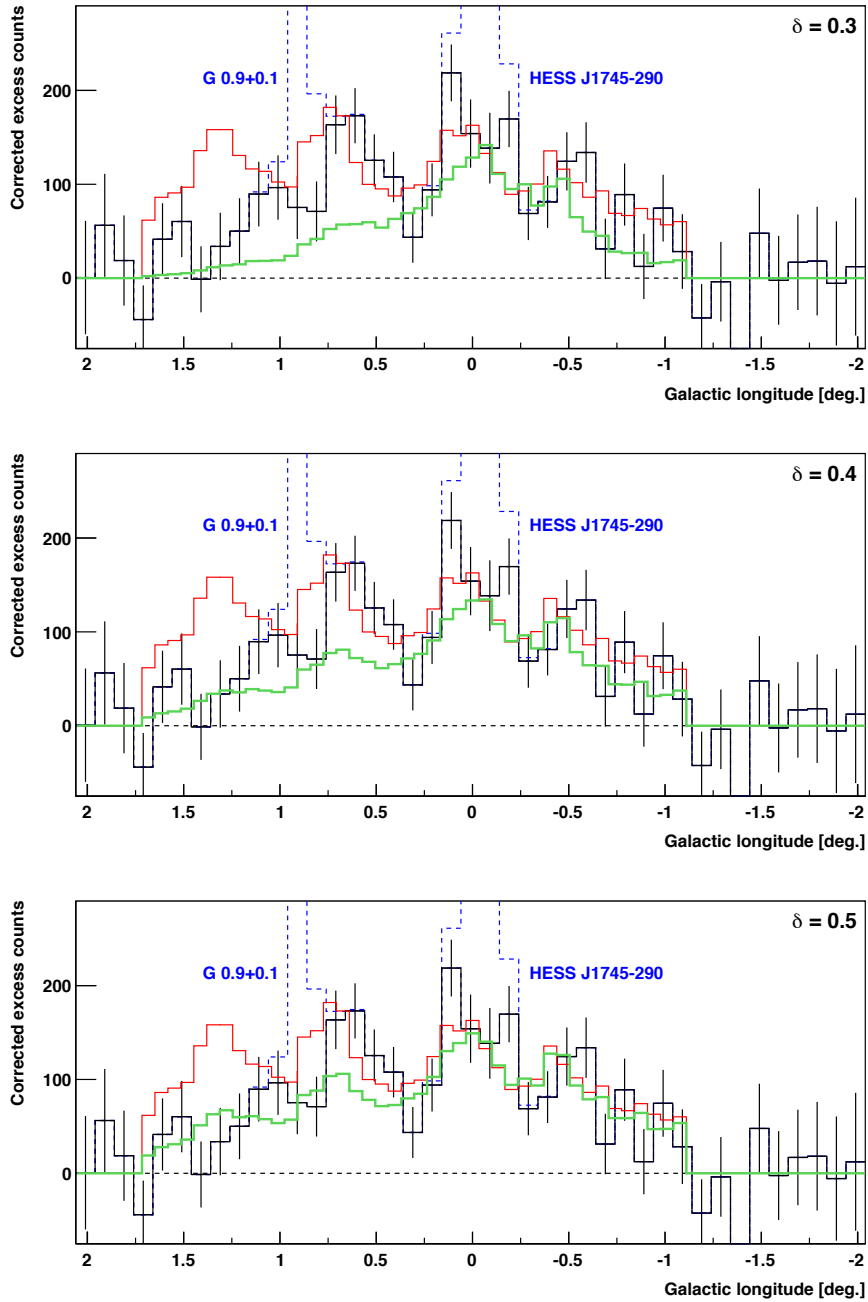


**Fig. 4.9:** Longitude profiles of  $\gamma$ -ray excess counts for  $|b| < 0.2^\circ$ , obtained from the simulation (green histogram) for  $D_{10} = 0.03 \text{ pc}^2/\text{yr}$  and different values of  $\delta$ . The black histogram shows the acceptance-corrected  $\gamma$ -ray counts measured with the H.E.S.S. instrument (data are taken from Aharonian et al. 2006a). The red curve depicts the density distribution of molecular gas. The energy threshold of the counts is 380 GeV.

above. For values of  $\delta \leq 0.2$ , the morphology of the excess obtained by the simulation does not match the characteristics of the measured data. For values of  $\delta \geq 0.3$ , the situation improves significantly. The best results seem to be obtained for  $\delta = 0.4/0.5$ . Here, the morphology of the  $\gamma$ -ray emission measured by H.E.S.S. is essentially reflected in the sim-

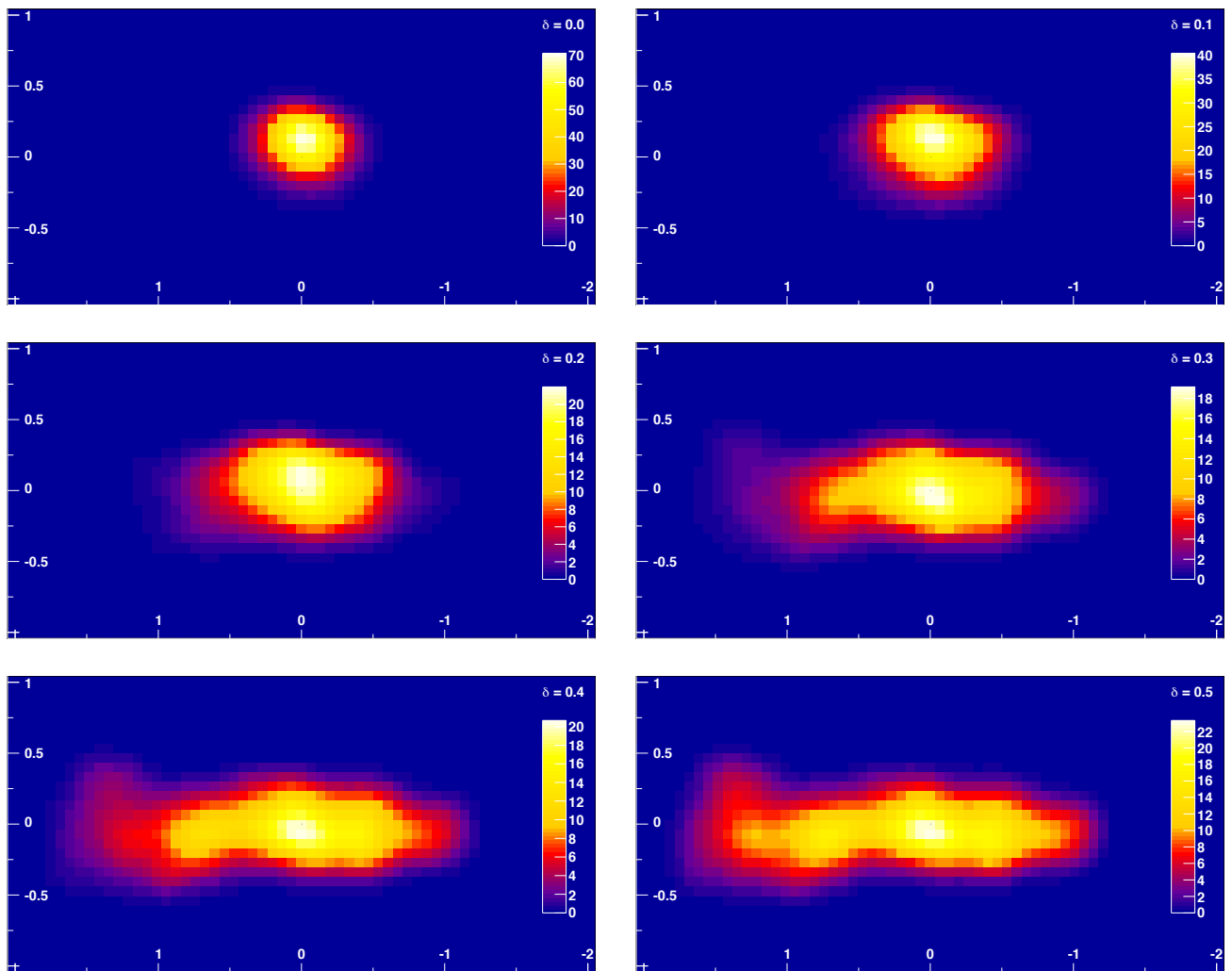


**Fig. 4.10:**  $\gamma$ -ray excess count maps of the Galactic Center region, calculated with the simulation for  $D_{10} = 0.03 \text{ pc}^2/\text{yr}$  and different values of  $\delta$ . Axes are Galactic longitude ( $x$ ) and Galactic latitude ( $y$ ). The energy threshold of these maps is 380 GeV and an observation time of 55 hours is assumed to match the conditions of the H.E.S.S. measurement presented by Aharonian et al. (2006a). The maps have been smoothed to match the H.E.S.S. point spread function.

ulated ones. Note that the absolute values of the excess counts obtained by the simulation (green histograms) depend on the values used for the effective area. Here, only approximative values can be used, as a detailed analysis of the H.E.S.S. data of the Galactic Center region was beyond the scope of this thesis. Hence, for  $\delta = 0.4/0.5$ , the diffusion model reproduces the morphology of the observed emission quite well, taking into account that the largest uncertainty here arises from the constructed density map of the molecular material.

Figure 4.10 shows the excess count maps calculated with the simulation as sky maps, smoothed with a Gaussian of a width of  $0.1^\circ$  to match the H.E.S.S. point spread function (the non-smoothed maps are shown in Fig. A.2). In these figures, it is again visible that only for  $\delta = 0.4/0.5$ , an extended morphology of the excess region as measured with the H.E.S.S. instrument can be reproduced by the simulation.

In summary, the derived results show that the simulation can reproduce the energy spectrum and the morphology of the measured diffuse  $\gamma$ -ray emission in substantial parts quite well for certain parameters. For this analysis, for the adopted value of  $D_{10} = 0.03 \text{ pc}^2/\text{yr}$ , a spectral index of  $\delta = 0.5$  is preferred against other values of the considered range  $\delta = 0.0 - 0.5$ , as for this value, the simulation output matches the measured spectrum quite well (in the sense of the defined  $\chi^2$ -fit) and essentially reproduces the morphology of the observed  $\gamma$ -ray emission. The shown results suggest that values significantly smaller than  $D_{10} = 0.03 \text{ pc}^2/\text{yr}$  cannot lead to a  $\gamma$ -ray excess as measured with the H.E.S.S. instrument, as protons would diffuse out of the central dense region too slowly, and the losses of particles would strongly increase. This statement will be discussed in more detail in the next section, in which the diffusion coefficients derived in this thesis (which are about 3 orders of magnitude smaller than  $D_{10} = 0.03 \text{ pc}^2/\text{yr}$ ) are applied to the simulation.

#### 4.2.2 Results for diffusion coefficients derived in this work

In this section, the diffuse  $\gamma$ -ray emission is simulated using the diffusion coefficients derived in this work. As mentioned above, only the values derived for the case of a purely turbulent magnetic field will be taken into account here due to the uncertainties in the description of the entire magnetic field configuration in the Galactic Center region (see Section 3.3.1). The diffusion coefficients are used as simulation input parameters in the form

$$\begin{aligned} D_{50}(E) &= (2.9 \times 10^{-5}) \text{ pc}^2/\text{yr} \left( \frac{E}{10 \text{ GeV}} \right)^{0.42} & \text{for } E \leq (4.1 \times 10^{14}) \text{ eV} \\ D_{50}(E) &= (2.2 \times 10^{-7}) \text{ pc}^2/\text{yr} \left( \frac{E}{10 \text{ GeV}} \right)^{0.88} & \text{for } E > (4.1 \times 10^{14}) \text{ eV} \end{aligned} \quad (4.11)$$

referring to the setting  $B_0 = 50 \mu\text{G}$ , and

$$\begin{aligned} D_{500}(E) &= (1.5 \times 10^{-5}) \text{ pc}^2/\text{yr} \left( \frac{E}{10 \text{ GeV}} \right)^{0.40} & \text{for } E \leq (3.8 \times 10^{15}) \text{ eV} \\ D_{500}(E) &= (3.0 \times 10^{-8}) \text{ pc}^2/\text{yr} \left( \frac{E}{10 \text{ GeV}} \right)^{0.88} & \text{for } E > (3.8 \times 10^{15}) \text{ eV} \end{aligned} \quad (4.12)$$

referring to the setting  $B_0 = 500 \mu\text{G}$ . These values are calculated from the non-rounded values of the parameter  $\text{Log}(D_{10})$ , obtained from the simulation of the numerical analysis in Section 3.3.2, without taking into account errors of the parameters (the reference values are given in Tab. 3.3). The given energies separating the two dynamical regimes are obtained from the corresponding values of the parameter  $\epsilon_{\text{break}}$ , see also Section 3.3.2. First, a discussion of the proton spectra after a tracking time of  $10^4$  years will be given, which will be followed by the discussion of the calculated  $\gamma$ -ray spectra and count maps.

#### Proton spectra

The energy spectra of the protons located inside the working environment after a tracking time of  $10^4$  years are shown in Fig. 4.11, together with the start spectrum at time  $t = 0$ . For both parametrizations  $D_{50}(E)$  and  $D_{500}(E)$ , an immense loss of particles of about 6 orders of magnitude occurs in the energy regime below the break energy, compared to the start spectrum. The vertical dashed lines indicate the break positions, which separate the two different dynamical regimes as discussed in Section 3.3.2. To get an idea of a time

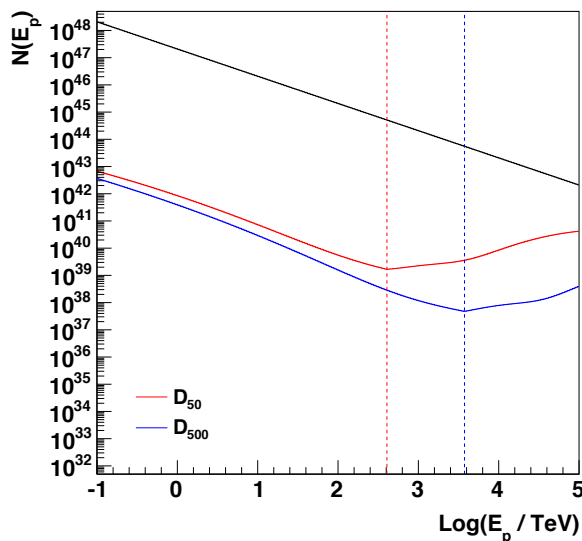


**Fig. 4.11:** Start proton spectrum at time  $t=0$  (black histogram) and proton spectra after a tracking time of  $t=10^4$  years. Here, the diffusion coefficients  $D_{50}(E)/D_{500}(E)$ , derived in this work, are applied (see Eq. 4.11/4.12). The quantity  $N(E_p)$  gives the number of particles at energy  $E_p$ , i.e. the number of particles integrated over the corresponding energy bin. Vertical dashed lines depict the break energies, which separate two dynamical regimes (see Section 3.3.2).

averaged density value of the ambient matter that is needed to account for such a loss of particles due to interaction processes, a small exemplary calculation can be carried out. Assuming a proton-proton cross-section of  $\sim 34$  mb (referring to an energy of 1 TeV) and applying Eq. 4.9 for a total time interval of  $10^4$  years, the result of this calculation gives a time averaged density of  $\overline{n_H(t)} = 4.2 \times 10^4 \text{ cm}^{-3}$ , assuming that only a fraction of  $10^{-6}$  of the originally injected particles survives the entire tracking time period. Hence, this outcome confirms the results of the simulation: if the protons rest in the central dense core directly around the origin of the working environment for the complete time interval, there will be substantial particle losses due to interaction processes. The influence of the spectral index  $\delta$  is again clearly visible in the shown spectra. Its value is approximately doubled after the break energy, respectively. The consequence is that the particles diffuse much faster with increasing energy, which finally leads to an increase in the number of particles as a function of energy, as the losses are therefore reduced compared to the lower energy range. Comparing the two different cases  $D_{50}$  and  $D_{500}$ , the loss of particles for  $D_{500}$  is slightly higher than the loss for  $D_{50}$ . This reflects the fact that for constant energy, the scale of movement of particles is more confined for higher magnetic field strengths than for lower ones. This in turn means that the particles stay for longer time in denser regions, which leads to more particle losses.

To gain deeper insight into the spatial distributions of the protons after  $10^4$  years, Fig. 4.12 shows the distribution of the particles along Galactic longitude as a function of particle energy  $E_p$ . In both shown cases, the protons are mainly confined to the very central region around the origin, due to the small values of the diffusion coefficients compared to the values in the previous section. To illustrate this point, one can for example analytically calculate the standard deviation  $\sigma = \sqrt{2D_{50}(E)t}$  after a time of  $10^4$  years. For an energy

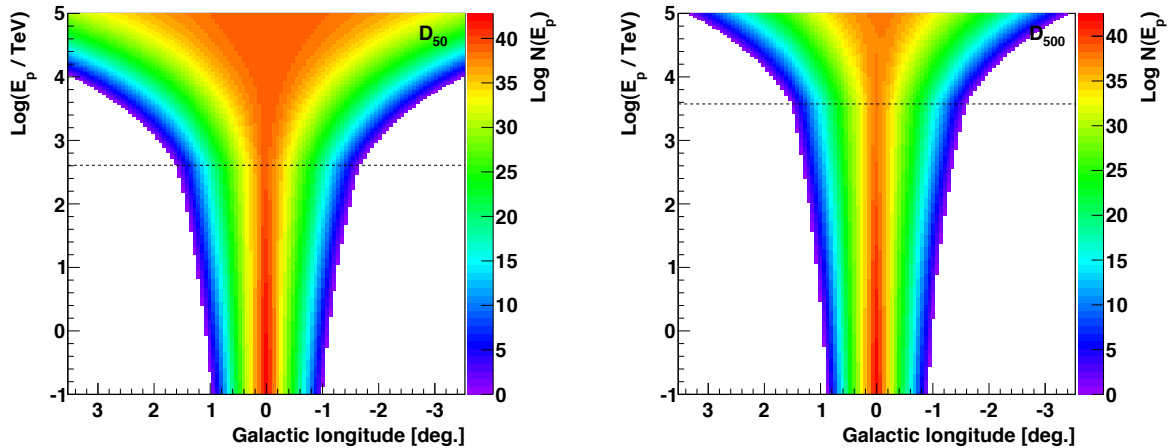


**Fig. 4.12:** Proton spectra  $N(E_p)$  along Galactic longitude after a total tracking time of  $10^4$  years, for diffusion coefficients  $D_{50}(E)$  and  $D_{500}(E)$ . Due to the small values of  $D_{10}$ , which are on a scale of  $10^{-5}$   $\text{pc}^2/\text{yr}$ , the particles are mainly confined to the very central region around the origin. The value refers to the dynamical regime below the break energy, which is indicated by the dashed horizontal lines, respectively.

of  $4 \times 10^{14}$  eV, which is slightly below the break energy, the result is  $\sigma \approx 7$  pc  $\approx 0.05^\circ$ . Compared to the bin width of 10 pc, this result indicates that most of the particles are confined to the central bin and its direct neighbors, reflecting the results shown in Fig. 4.12. Furthermore, one can observe that for energies above the break, the width of the distributions broadens much faster as a function of energy than below the break, due to the approximately doubled values of the spectral indices  $\delta$  there. Comparing the figures for  $D_{50}(E)$  and  $D_{500}(E)$ , a comparison of the width of the distributions for constant energy again shows that particles diffuse faster for  $B_0 = 50$   $\mu\text{G}$  than for  $B_0 = 500$   $\mu\text{G}$ , as described above.

Already at this point, the presented results show that the observed  $\gamma$ -ray excess cannot be reproduced by the applied diffusion coefficients due to the large losses of particles and their confinement to the very central region around the center of the Galaxy.

#### $\gamma$ -ray spectra and excess count maps

The  $\gamma$ -ray spectra, calculated at  $t = 10^4$  years from the presented proton distributions, are shown in Fig. 4.13. The black histograms show the uncorrected spectra, calculated by the simulation, whereas red curves are curves of these primary output spectra fitted to the H.E.S.S. measurement (blue dots). The fits were carried out with the introduced  $\chi^2$  method (see Eq. 4.10). Again, separate power-law fits are performed to the simulated output spectra to obtain an analytical description in the energy regime  $-1 < (E/\text{TeV}) < 1.3$ . The obtained values of both the  $\chi^2$  minimization and the power-law fit are summarized for  $D_{50}(E)$  and  $D_{500}(E)$  in Tab. 4.2.

With values of  $\alpha = 142.89$  ( $D_{50}$ ) and  $\alpha = 1206.97$  ( $D_{500}$ ), the normalization factors of the  $\chi^2$  optimization are much larger than in the previous section, in which the simulated spectra for  $D_{10} = 0.03$   $\text{pc}^2/\text{yr}$  are obtained in the same order of magnitude as the measured

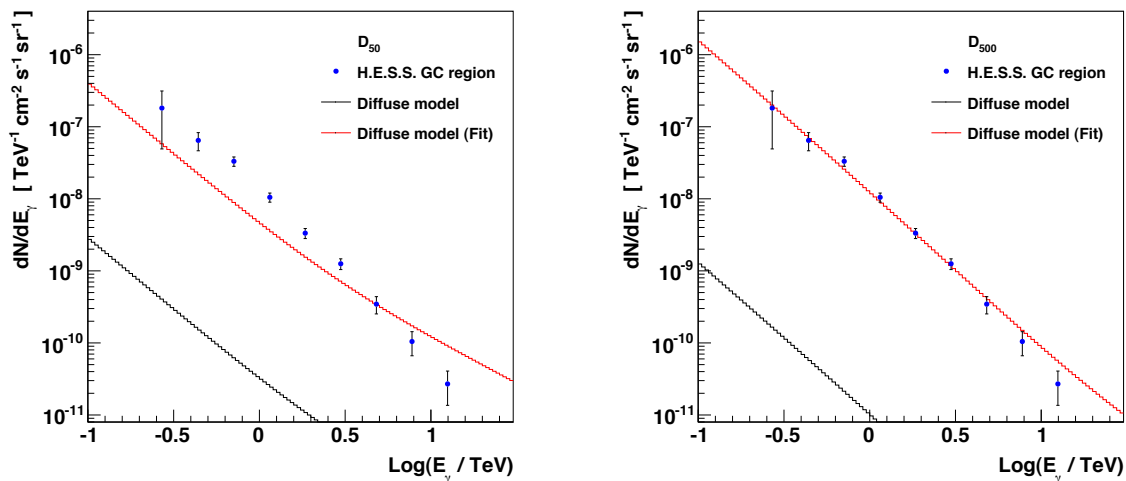


**Fig. 4.13:**  $\gamma$ -ray flux in the Galactic Center region obtained from the simulation for diffusion coefficients  $D_{50}(E)$  and  $D_{500}(E)$ . The shown spectra refer to a region  $|l| < 0.8^\circ$  and  $|b| < 0.3^\circ$  to allow comparison to the H.E.S.S. data (Aharonian et al. 2006a), shown using blue dots. Black curves correspond to uncorrected spectra directly obtained from the simulation, whereas red curves depict fit curves of this primary output spectra to the flux measured with the H.E.S.S. instrument.

**Table 4.2:** Fit parameters of the  $\chi^2$ -fit, as introduced in Eq. 4.10. The spectral indices  $\Gamma_\gamma$  are obtained from separate power law fits to the spectra calculated with the simulation, assuming that these can be described by a simple power law in the energy regime  $-1 < (E/\text{TeV}) < 1.3$ .

	$\alpha$	$\chi^2/\text{d.o.f.}$	p-value	$\Gamma_\gamma$
$D_{50}$	142.89	12.08	$2 \times 10^{-17}$	1.7
$D_{500}$	1206.97	1.33	0.22	2.1

$\gamma$ -ray flux. In contrast, the results here demand a correction of the originally assumed energy amount to be spent into acceleration processes ( $10^{50}$  erg) by about two or three orders of magnitude. Hence, assuming 10% conversion efficiency for acceleration, the total required source energies exceed the usually assumed explosion energy of supernovae ( $\sim 10^{51}$  erg) by the same amount. Thus, the immense losses of protons during the propagation for the applied diffusion coefficients, as discussed above, are reflected in the results of the  $\gamma$ -ray spectra.

The slope of the obtained spectrum does obviously not match the measured data points for the case of  $D_{50}(E)$ , and due to energy-dependent influences, the spectral form cannot exactly be described by a power law. For the case  $D_{500}(E)$ , the slope of the spectrum seems to fit better to the measured data points. However, as already discussed, the normalization factor  $\alpha$  here is again one order of magnitude larger than for the case of  $D_{50}(E)$ . The presented results are essentially reflected by the derived fit parameters, given in Tab. 4.2.

In the following, a discussion of the corresponding  $\gamma$ -ray excess count maps, obtained from the simulation, is given. The calculated excess counts are shown as longitude profiles in Fig. 4.14 (green histograms). The normalization factors  $\alpha$  are taken into account for the calculation. As expected, the excess region is essentially confined to the central bin and

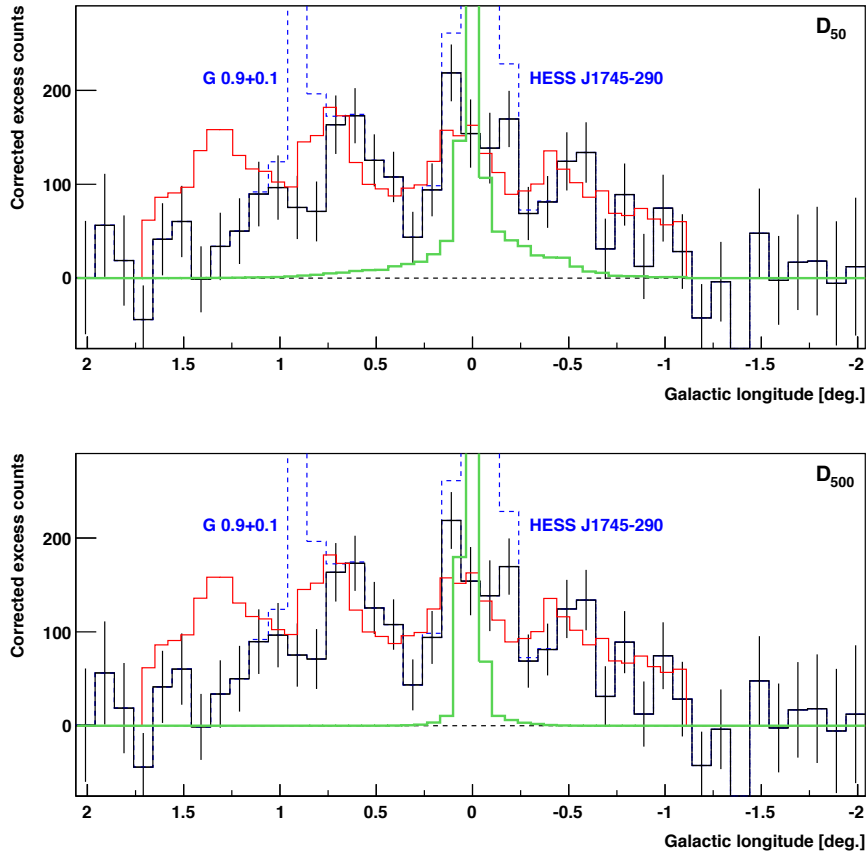


**Fig. 4.14:** Longitude profiles of  $\gamma$ -ray excess counts for  $|b| < 0.2^\circ$ , obtained from the simulation (green histogram) for  $D_{50}(E)$  and  $D_{500}(E)$ . The black histogram shows the acceptance-corrected  $\gamma$ -ray counts measured with the H.E.S.S. instrument (data are taken from Aharonian et al. 2006a). The red curve depicts the density distribution of molecular gas. The energy threshold of the counts is 380 GeV.

its neighbors. This feature is more enhanced for the  $D_{500}(E)$  data than for the  $D_{50}(E)$  data. In the longitude projection, the central bin ( $l = 0^\circ$ ) includes  $\sim 700$  counts for  $D_{50}(E)$  and  $\sim 2400$  counts for  $D_{500}(E)$ . Compared to the direct neighbor bins with contents  $< 200$  counts, this shows that the emissivity drops significantly within the distance of only one bin from the center (bin width  $\sim 0.07^\circ$ ). Thus, from the morphology of the obtained excess, one can finally conclude that for the applied diffusion coefficients and a total tracking time of  $10^4$  years, a spatially extended diffuse  $\gamma$ -ray excess as observed with the H.E.S.S. instrument cannot be produced by diffusing charged particles which are released by a single impulsive ejection of a central source.

Additionally, Fig. 4.15 shows the  $\gamma$ -ray excess count maps as sky maps. As already visible in the longitude profiles, the emission regions are confined to high-intense regions looking like point sources at the Galactic Center. The center of the emission regions is slightly shifted towards positive values in Galactic longitude ( $\sim 0.07^\circ$ ), due to asymmetries in the density map representing the ambient matter. The central emission regions have a diameter (full width half maximum) of approximately  $0.2^\circ$  after smoothing, respectively. The non-smoothed maps are shown in Fig. A.3.

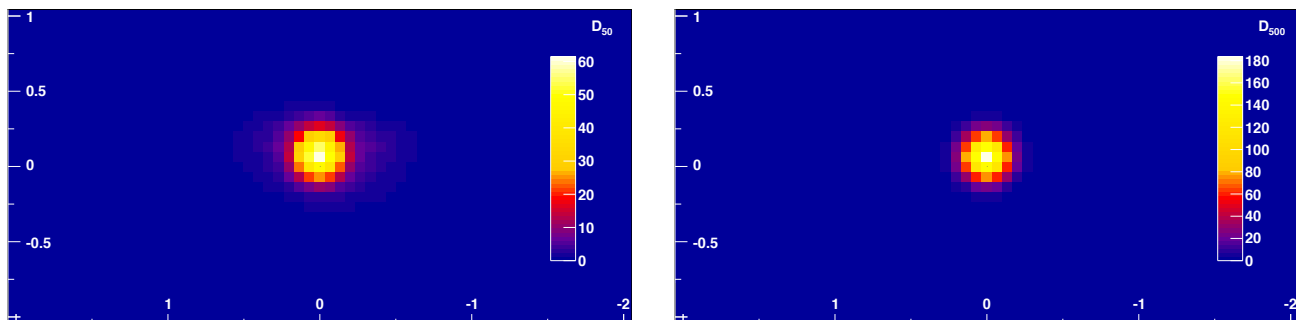


**Fig. 4.15:**  $\gamma$ -ray excess count maps of the Galactic Center region, simulated with  $D_{50}(E)$  and  $D_{500}(E)$ . Axes are Galactic longitude ( $x$ ) and Galactic latitude ( $y$ ). The energy threshold of the maps is 380 GeV and an observation time of 55 hours is assumed to match the conditions of the H.E.S.S. measurement presented by Aharonian et al. (2006a). The maps have been smoothed to match the H.E.S.S. point spread function.

The shown results are, however, compatible with those derived by Wommer et al. (2008). These authors worked with the same numerical formalism in order to track particles in turbulent magnetic fields, not directly deriving diffusion coefficients but similar outline parameters to describe the time development of the proton distribution. Using similar conditions, the  $\gamma$ -ray count map derived by these authors shows TeV emission centered on Sgr A\*, with a spatial extension of only a fraction of a degree. From their simulation, the authors concluded that the  $\gamma$ -ray emissivity should drop by a factor of  $\sim 2$  within a distance of about  $0.1^\circ$ . These results are very similar to the ones derived in this section, as discussed above.

Hence, the question arises whether a time period longer than  $10^4$  years could lead to a more extended emission region, applying the diffusion coefficient  $D_{50}(E)$  to the simulation. However, regarding the fact that particle losses would again increase, it can be expected that the requirement of unreasonable source energies would be the result of such an approach, taking into account that for  $10^4$  years, the normalization factor  $\alpha$  is already  $\alpha = 142.98$ , as discussed above. To validate this assumption, simulation runs using  $D_{50}(E)$  were performed for total tracking times of  $10^5$ ,  $10^6$  and  $10^7$  years. The results show that for none of these time scales, a diffuse  $\gamma$ -ray excess similar to the one observed with the H.E.S.S. instrument is obtained by the simulation. Firstly, for all applied time periods, the slope of the calculated energy spectra is much flatter than suggested by the measured data. For the reduced  $\chi^2$ , values of  $\chi^2/8 \geq 17.64$  are obtained. Secondly, the morphology of the obtained excess does not fit to the observed one for any of the applied time steps. The emission region extends for the longer time periods, but due to the immense particle losses, the obtained structures show a strong glowing contour, with nearly no emission from the inner volume. Thirdly, the obtained normalization factors  $\alpha$  are at least of the order of magnitude of  $10^4$ , up to  $10^{10}$ , which confirms the above discussed assumption of unreasonably high required source energies.

In summary, the results of this section show that for the diffusion coefficients  $D_{50}(E)$  and  $D_{500}(E)$ , the diffuse  $\gamma$ -ray emission at the Galactic Center region, as observed with the H.E.S.S. instrument, cannot be reproduced assuming the hadronic diffusion scenario as its origin. The diffusion coefficients  $D_{50}(E)$  and  $D_{500}(E)$  thereby refer to diffusion coefficients derived in this thesis, for the setting  $B_0 = 50 \mu\text{G}$  and  $B_0 = 500 \mu\text{G}$  under the assumption of

a purely turbulent magnetic field (see Section 3.3.2). This means the diffusion coefficients are derived from the movement of charged particles in a turbulent magnetic field with an energy density equal to a homogeneous magnetic field of strength  $B_0$  (see Section 3.2).

## 5 Conclusion and outlook

The aim of this thesis was to assess the validity of the hadronic diffusion scenario as origin of the diffuse very-high-energy  $\gamma$ -ray emission from the Galactic Center region which was discovered by the H.E.S.S. experiment in 2006 (Aharonian et al. 2006a). There are two different approaches to analyzing the hypothesis that the detected TeV  $\gamma$ -rays arise from interaction processes of highly energetic hadrons with ambient matter, whereby the acceleration of the diffusing particles is assumed to have taken place in a single central power source. As discussed in Section 2.2, the results of both approaches show disagreement. Working under the assumption that the hadronic diffusion scenario is the correct model to describe the observations, some authors derived the best-fit parameters for the diffusion coefficient to match the measured data (e.g. Nekrasov 2010; Dimitrakoudis et al. 2009; Büsching et al. 2007). In contrast to that, Wommer et al. (2008) worked with an alternative approach, in which particles are directly tracked in turbulent magnetic fields. The results thereby obtained suggest that particles diffuse away from a central source too slowly to be able to produce an extended emission as observed with the H.E.S.S. instrument. Hence, this outcome implies that diffusion coefficients cannot be as large as derived by the aforementioned authors.

To enable a consistent treatment of the problem, the first part of this thesis dealt with a numerical approach to tracking charged particles in turbulent magnetic fields. From the output measures of the tracking of ensembles of particles, diffusion coefficients were derived with regard to the physical conditions in the Galactic Center region. This was done for a turbulent magnetic field, superimposed by a static background component, and for a purely turbulent magnetic field. The maximum turbulent wavelength was set to  $\lambda_{\max} = 1 \text{ pc}$ , and magnetic field strengths of  $B_0 = 50 \mu\text{G}$  and  $B_0 = 500 \mu\text{G}$  were applied. For the case of a turbulent magnetic field superimposed by a static background component,  $B_0$  denotes the field strength of the homogeneous component, and the turbulent part was defined in such a way that the energy density of the homogeneous component and the turbulent component have the same value. For the case of a purely turbulent field, the energy density of the turbulent field was defined to be equal to the one of a homogeneous magnetic field of strength  $B_0$ . The turbulent fields were generated assuming Kolmogorov turbulence, i.e. the spectral energy density of the turbulent field is assumed to follow a power law with a spectral index of  $\Gamma = 5/3$ .

In general, the derived results for the diffusion coefficient as a function of energy are consistent with the results obtained by other authors (e.g. Fatuzzo et al. 2010; Fatuzzo & Melia 2012). For the case of a turbulent field superimposed by a static background component, a break in the energy dependence of the diffusion coefficient is observed for diffusion across the underlying homogeneous component. For the case of a purely turbulent field, such a break is observed, too. In both cases, its position is to be found at  $R_g \sim 0.01\lambda_{\max}$ , whereby  $R_g$  denotes the gyroradius of the particles in a homogeneous magnetic field of strength  $B_0$ . These results are consistent with those of Fatuzzo et al. (2010) and show that particle diffusion behaves differently above and below the break energy.

The obtained data are well described by the standard scaling law  $D(E) = D_{10} (E/10 \text{ GeV})^\delta$ ,

with different spectral indices  $\delta$  above and below the break.  $D_{10}$  denotes the value of the diffusion coefficient at an energy of 10 GeV. The values obtained for this quantity, given as  $\text{Log}[D_{10}/(\text{cm}^2/\text{s})]$ , range from about 24.6 to 25.9, whereby higher values refer to the case of diffusion along the direction of the homogeneous background field. Thus, for diffusion across the underlying homogeneous component or for diffusion in a purely turbulent field, the obtained values for  $D_{10}$  are about one order of magnitude smaller than the lower border of the usually assumed range  $D_{10} \sim 10^{26} - 10^{28} \text{ cm}^2/\text{s}$  (see e.g. Aharonian & Atoyan 1996; Gabici et al. 2009).

The obtained spectral indices  $\delta$  are generally in good agreement with the usually quoted range of  $\delta \sim 0.3 - 0.6$  (e.g. Aharonian & Atoyan 1996; Strong et al. 2007). For the dynamical regimes below the break energy, the obtained values are compatible with  $\delta = 2 - \Gamma = 1/3$ . This is the value expected from standard theory of particle diffusion for a spectral index of the turbulent magnetic field of  $\Gamma = 5/3$  for the applied Kolmogorov turbulence. In the regime above the break, however, significantly larger values are obtained, assuming a power-law dependence of the diffusion coefficient as a function of energy.

In the second part of this thesis, a simulation was developed to model the observed diffuse  $\gamma$ -ray emission from the Galactic Center region, assuming the hadronic diffusion scenario as its origin. Using finite difference methods, the diffusion equation was discretized and particles were tracked on a discrete three-dimensional computing grid. In such a formalism, the diffusion coefficient enters as free input parameter. A density map of the molecular environment of the Galactic Center was embedded within the three-dimensional working environment to model the interaction processes of the accelerated particles with the molecular clouds. Particle losses during the applied propagation time of  $10^4$  years were taken into account. The initial energy spectrum of the protons, which were used as representatives for the diffusing hadrons, was assumed to follow a power with a spectral index of  $\Gamma_p = 2$ . The considered energy range is  $10^{11} - 10^{17} \text{ eV}$ . Furthermore, it was assumed that the protons were released by a single impulsive ejection of a source which is located at the origin of the Galactic coordinate system ( $l=b=0^\circ$ ).

First, the simulation was performed choosing  $D_{10} = 10^{28} \text{ cm}^2/\text{s} \approx 0.03 \text{ pc}^2/\text{yr}$  in combination with a small parameter scan of the spectral index  $\delta = 0.0, \dots, 0.5$ . The obtained results were compared with the H.E.S.S. measurement as given by Aharonian et al. (2006a). Fits of the calculated spectra to the measured one using the  $\chi^2$ -method achieve estimates for the total required source energies, with values of  $0.32 \times 10^{51} \text{ erg} - 5.72 \times 10^{51} \text{ erg}$ . An analysis of the morphology of the simulated excess region shows that for values of  $\delta = 0.4/0.5$ , the essential features of the observed  $\gamma$ -ray emission can be well reproduced by the simulation. The favored spectral index is  $\delta = 0.5$ , as for this value the results of the simulation match the measured spectrum and the observed morphology of the diffuse emission quite well.

The parameter set  $\Gamma_p = 2$ ,  $D_{10} = 0.03 \text{ pc}^2/\text{yr}$  and  $\delta = 0.5$  is in agreement with the allowed 95% confidence regions of the parameter scan of the two-dimensional model performed by Nekrasov (2010). For the three-dimensional model, the parameter set just missed the 95% confidence regions. However, it has to be noted that the results derived by Nekrasov (2010) are based on an individual analysis of the H.E.S.S. data of the Galactic Center region and the obtained flux values might therefore differ from the ones reported by Aharonian et al. (2006a). The estimated range derived by Büsching et al. (2007),  $D_{10} = 0.04 \text{ pc}^2/\text{yr} - 0.2 \text{ pc}^2/\text{yr}$ , assuming  $\delta = 0.6$  and  $\Gamma_p = 2.29$ , is very similar to the parameter set given above. The results reported by Dimitrakoudis et al. (2009), in contrast, include higher values. For  $\delta = 0.3, \dots, 0.6$ ,  $2.1 \leq \Gamma_p \leq 2.3$ , these authors

---

give a typical value of  $D(E = 3.2 \text{ TeV}) = (3.0 \pm 0.2) \text{ pc}^2/\text{yr}$ , compared to a value of  $D(E = 3.2 \text{ TeV}) = 0.54 \text{ pc}^2/\text{yr}$  for the best fitting parameter set tested in this work. However, the results of the first run show that for the choice of  $D_{10} = 0.03 \text{ pc}^2/\text{yr}$ , the developed simulation can reproduce the observed diffuse  $\gamma$ -ray excess quite well, in agreement with the results of other authors working under the assumption of the validity of the diffusion hypothesis.

In contrast, a totally different result was found applying the diffusion coefficients derived in this work with values of  $D_{10} \approx 10^{25} \text{ cm}^2/\text{s} \approx 3 \times 10^{-5} \text{ pc}^2/\text{yr}$ . For these diffusion coefficients, the derived simulated emission after  $10^4$  years has characteristics of a point source instead of a spatially extended emission region, because the particles diffuse away from their point of origin at the Galactic Center too slowly. Moreover, immense particle losses during propagation are observed, leading to required source energies of about  $10^{53} \text{ erg}$  to explain the  $\gamma$ -ray flux observed by H.E.S.S. Further studies show that also for larger time scales up to  $10^7$  years, an emission as observed with the H.E.S.S. instrument cannot be reproduced by the simulation applying the diffusion coefficients derived in this work. The slopes of the obtained energy spectra are much flatter than suggested by the measured data points, and source energies of at least  $10^{55} \text{ erg}$  would be required to obtain a flux of the same order of magnitude as measured. Additionally, due to immense particle losses in the inner volume, the morphology of the simulated  $\gamma$ -ray emission does not fit the observed one.

Typical errors of the derived values of the quantity  $\text{Log}[D_{10}/(\text{cm}^2/\text{s})]$  are about  $\pm 1$ . Hence, uncertainties of about one order of magnitude must be taken into account, which, however, cannot explain the observed discrepancies. Regarding model parameters for the derivation of the diffusion coefficients, a magnetic field strength of  $B_0 = 50 \mu\text{G}$  was chosen for the less restricting scenario, in agreement with the lower limit for the magnetic field strength of the Galactic Center region as given by Crocker et al. (2010). The second important parameter with considerable influence on the dynamics of charged particles in turbulent magnetic fields, the value of the maximum turbulent wavelength with respect to the particles gyroradius, was set to 1 pc. The choice of this value had already been suggested as a reasonable estimate by other authors (Fatuzzo et al. 2010; Fatuzzo & Melia 2012). Furthermore, a change of three orders of magnitude in the derived diffusion coefficients is yet far away from the observed influence of  $\lambda_{\text{max}}$ , assuming an uncertainty of one order of magnitude for its value.

Hence, the results derived in this work tend to preclude the hadronic diffusion scenario as possible origin of the diffuse  $\gamma$ -ray emission from the Galactic Center region, as only diffusion coefficients which are about three orders of magnitude larger than the derived ones could achieve a reasonable result. The finding that in an environment like the Galactic Center region, particles diffuse away from a single source too slowly to account for a widely extended emission region is in agreement with the conclusion of Wommer et al. (2008).

Alternative scenarios which could lead to the observed diffuse  $\gamma$ -ray emission have already been suggested. Essentially, the idea of a production of  $\gamma$ -rays via interaction processes of relativistic cosmic rays with the ambient material remains, due to the observed correlation between the morphology of the diffuse TeV emission and the density distribution of the ambient matter. The approach of assessing the feasibility of in situ particle acceleration by magnetic turbulence in the Galactic Center region is pursued by Fatuzzo & Melia (2012, 2014). Another scenario assumes that a powerful wind, which is launched by the

Galactic Center, advects previously accelerated particles out of the inner region with a constant velocity  $v_{\text{wind}}$  of a few 100 km/s (e.g. Crocker et al. 2011). In such a scenario, particle transport would become energy independent, meaning that transport would not change the slope of the initial injection spectrum. The future Cherenkov Telescope Array (see e.g. Actis et al. 2011) will enable a further improvement of the understanding of the particle astrophysics of the Galactic Center region. Due to the unprecedented sensitivity, energy coverage and angular resolution of this instrument, it will presumably be possible to distinguish between the different addressed scenarios by energy-dependent morphological analysis and spatially resolved spectrum reconstruction.

# Appendix

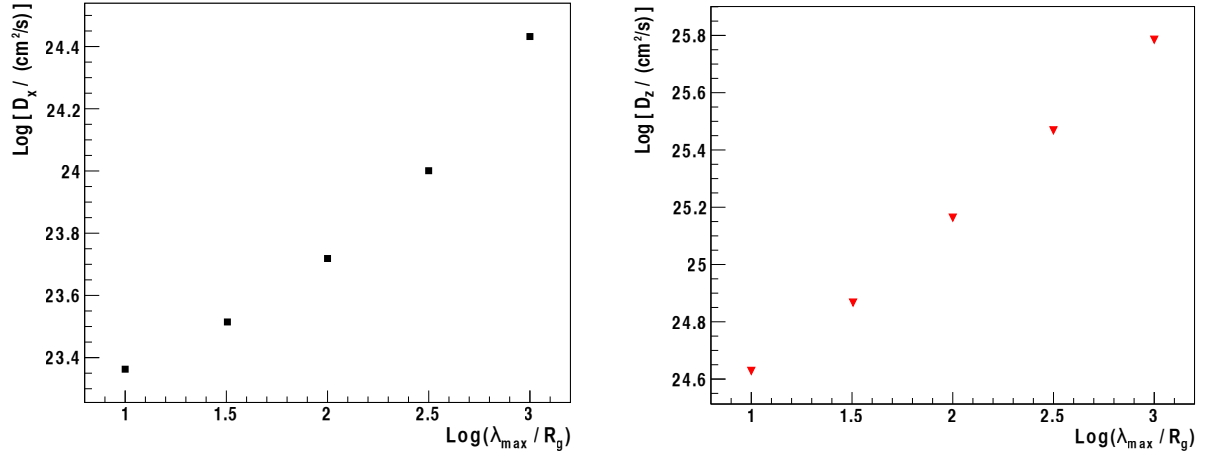


**Fig. A.1:** Diffusion coefficients in  $x$  (left) and  $z$  (right) direction as a function of  $\lambda_{\text{max}}$ . The derived values increase by about one order of magnitude when varying the value of  $\lambda_{\text{max}}$  from  $10R_g$  up to  $1000R_g$ . The values in  $y$  direction are identical to those in  $x$  direction apart from statistical fluctuations and not shown explicitly. These diffusion coefficients have been derived within the Bachelor thesis of Oberndörfer (2014). The particle energy was set to 1 TeV, and  $B_0$  was set to  $B_0 = 50 \mu\text{G}$ .

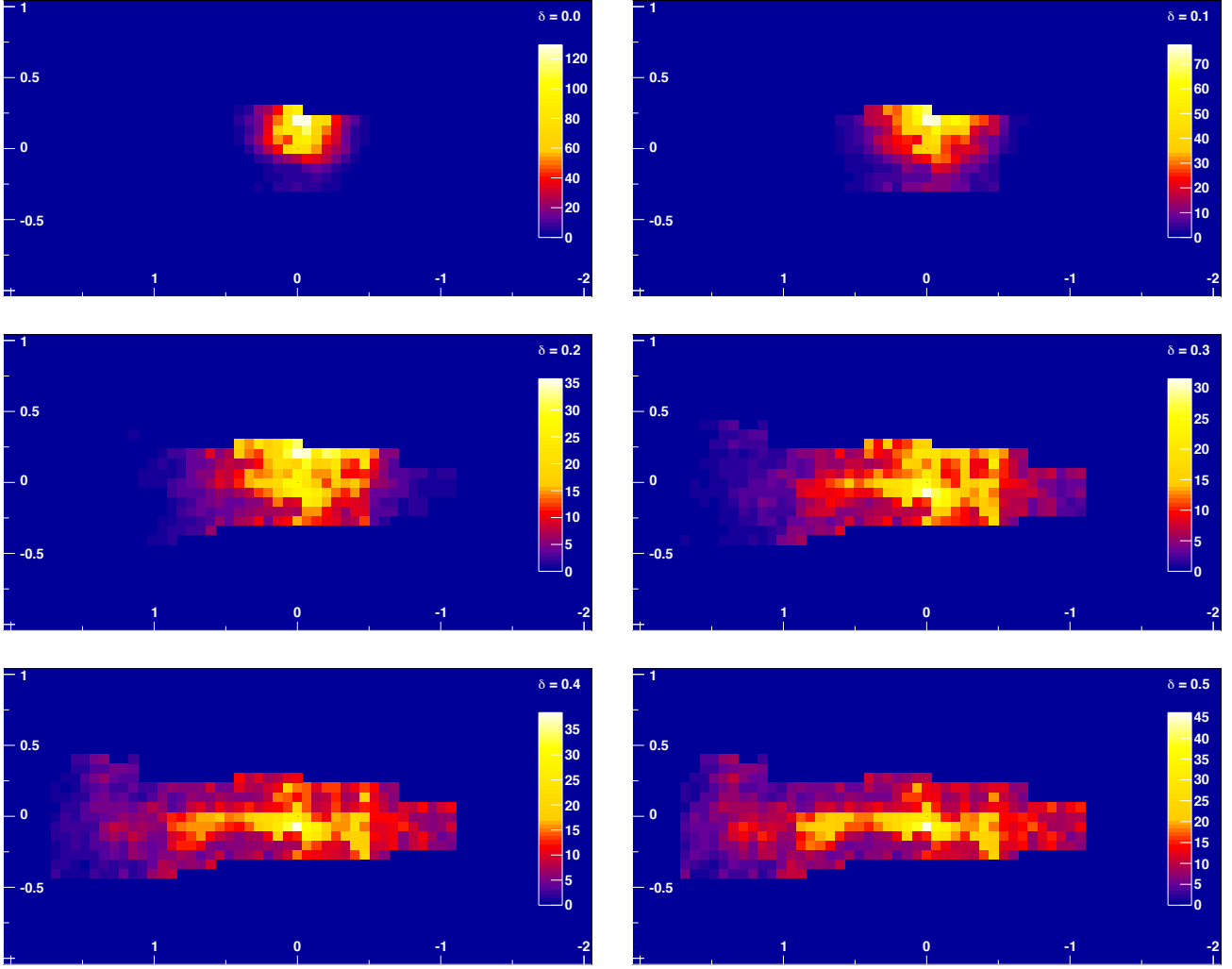


**Fig. A.2:** Non-smoothed  $\gamma$ -ray excess count maps of the Galactic Center region, calculated with the simulation for  $D_{10} = 0.03 \text{ pc}^2/\text{yr}$  and different values of  $\delta$ .

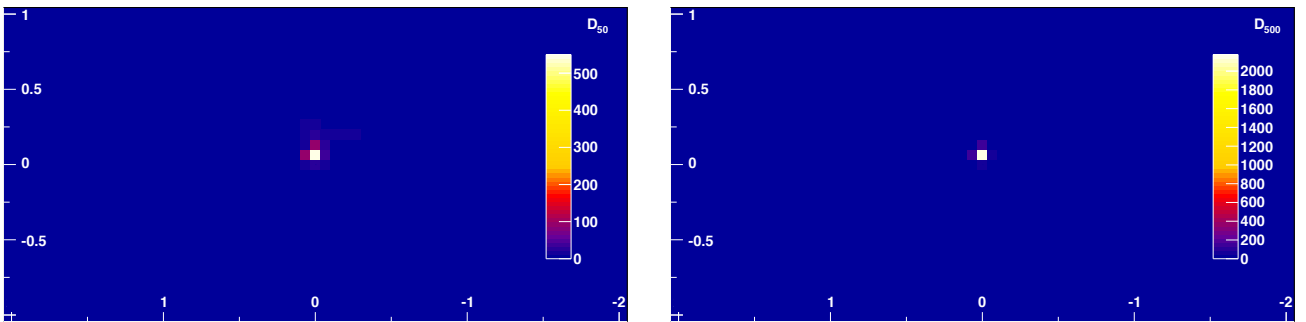


**Fig. A.3:** Non-smoothed  $\gamma$ -ray excess count maps of the Galactic Center region, simulated with  $D_{50}(E)$  and  $D_{500}(E)$ .

The figures Fig. A.2 and Fig. A.3 show the non-smoothed  $\gamma$ -ray excess count maps, calculated with the simulation. Axes are Galactic longitude (x) and Galactic latitude (y). The energy threshold of these maps is 380 GeV and an observation time of 55 hours is assumed.

# Bibliography

- Actis, M., Agnetta, G., Aharonian, F., et al. 2011, *Experimental Astronomy*, 32, 193
- Aharonian, F., Akhperjanian, A. G., Anton, G., et al. 2009, *A&A*, 503, 817
- Aharonian, F., Akhperjanian, A. G., Aye, K.-M., et al. 2005a, *A&A*, 432, L25
- Aharonian, F., Akhperjanian, A. G., Aye, K.-M., et al. 2005b, *Science*, 307, 1938
- Aharonian, F., Akhperjanian, A. G., Aye, K.-M., et al. 2004, *A&A*, 425, L13
- Aharonian, F., Akhperjanian, A. G., Barres de Almeida, U., et al. 2008, *A&A*, 483, 509
- Aharonian, F., Akhperjanian, A. G., Bazer-Bachi, A. R., et al. 2006a, *Nature*, 439, 695
- Aharonian, F., Akhperjanian, A. G., Bazer-Bachi, A. R., et al. 2006b, *Physical Review Letters*, 97, 221102
- Aharonian, F., Akhperjanian, A. G., Bazer-Bachi, A. R., et al. 2006c, *A&A*, 457, 899
- Aharonian, F. A. & Atoyan, A. M. 1996, *A&A*, 309, 917
- Bakunin, O. 2008, *Turbulence and Diffusion: Scaling Versus Equations*, Springer Verlag Berlin Heidelberg
- Bally, J., Stark, A. A., Wilson, R. W., & Henkel, C. 1987, *ApJS*, 65, 13
- Bolatto, A. D., Wolfire, M., & Leroy, A. K. 2013, *ARA&A*, 51, 207
- Boldyrev, S. & Yusef-Zadeh, F. 2006, *ApJ*, 637, L101
- Büsching, I., de Jager, O. C., & Snyman, J. 2007, *ApJ*, 656, 841
- Casse, F., Lemoine, M., & Pelletier, G. 2002, *Phys. Rev. D*, 65, 023002
- Chuss, D. T., Davidson, J. A., Dotson, J. L., et al. 2003, *ApJ*, 599, 1116
- Crocker, R. M., Jones, D. I., Aharonian, F., et al. 2011, *MNRAS*, 413, 763
- Crocker, R. M., Jones, D. I., Melia, F., Ott, J., & Protheroe, R. J. 2010, *Nature*, 463, 65
- Dimitrakoudis, S., Mastichiadis, A., & Geranios, A. 2009, *Astroparticle Physics*, 31, 13
- Fatuzzo, M. & Melia, F. 2012, *ApJ*, 750, 21
- Fatuzzo, M. & Melia, F. 2014, *ApJ*, 784, 131
- Fatuzzo, M., Melia, F., Todd, E., & Adams, F. C. 2010, *ApJ*, 725, 515
- Ferrière, K. 2009, *A&A*, 505, 1183
- Gabici, S., Aharonian, F. A., & Casanova, S. 2009, *MNRAS*, 396, 1629
- Giacalone, J. & Jokipii, J. R. 1994, *ApJ*, 430, L137
- Guesten, R. & Henkel, C. 1983, *A&A*, 125, 136

- Güsten, R. & Philipp, S. D. 2004, in *The Dense Interstellar Medium in Galaxies*, ed. S. Palfzner, C. Kramer, C. Staubmeier, & A. Heithausen, 253
- Hartman, R. C., Bertsch, D. L., Bloom, S. D., et al. 1999, *ApJS*, 123, 79
- Hinton, J. A. & Hofmann, W. 2009, *ARA&A*, 47, 523
- Kelner, S. R., Aharonian, F. A., & Bugayov, V. V. 2006, *Phys. Rev. D*, 74, 034018
- Kosack, K., Badran, H. M., Bond, I. H., et al. 2004, *ApJ*, 608, L97
- Longair, M. S. 2011, *High Energy Astrophysics*, Cambridge University Press
- Maeda, Y., Baganoff, F. K., Feigelson, E. D., et al. 2002, *ApJ*, 570, 671
- Mayer-Hasselwander, H. A., Bertsch, D. L., Dingus, B. L., et al. 1998, *A&A*, 335, 161
- Nekrassov, D. 2010, Dissertation, A detailed study of The H.E.S.S. data from the Galactic Center region, Combined Faculties for the Natural Sciences and for Mathematics, Ruperto-Carola University, Heidelberg, Germany
- Oberndörfer, M. 2014, Bachelor thesis, Simulationsstudien zu diffusem Teilchentransport in kosmischen Magnetfeldern, Erlangen Center for Astroparticle Physics, Lehrstuhl für Experimentalphysik, Friedrich-Alexander Universität, Erlangen, Germany
- Oka, T., Hasegawa, T., Sato, F., Tsuboi, M., & Miyazaki, A. 1998, *ApJS*, 118, 455
- O'Sullivan, S., Reville, B., & Taylor, A. M. 2009, *MNRAS*, 400, 248
- Press, W. H., Flannery, B. P., & Teukolsky, S. A. 1986, *Numerical recipes. The art of scientific computing*, Cambridge University Press
- Sawada, T., Hasegawa, T., Handa, T., & Cohen, R. J. 2004, *MNRAS*, 349, 1167
- Strong, A. W., Moskalenko, I. V., & Ptuskin, V. S. 2007, *Annual Review of Nuclear and Particle Science*, 57, 285
- TeVCat. 2014, online data base for TeV Astronomy, <http://tevcat.uchicago.edu/>
- The HESS Collaboration: Acero et al. 2009, arXiv e-prints
- Tsuboi, M., Handa, T., & Ukita, N. 1999, *ApJS*, 120, 1
- Tsuchiya, K., Enomoto, R., Ksenofontov, L. T., et al. 2004, *ApJ*, 606, L115
- Walmsley, C. M., Guesten, R., Angerhofer, P., Churchwell, E., & Mundy, L. 1986, *A&A*, 155, 129
- Wang, Q. D., Lu, F. J., & Gotthelf, E. V. 2006, *MNRAS*, 367, 937
- Weekes, T. C., Cawley, M. F., Fegan, D. J., et al. 1989, *ApJ*, 342, 379
- Wommer, E., Melia, F., & Fatuzzo, M. 2008, *MNRAS*, 387, 987
- Yusef-Zadeh, F., Morris, M., & Chance, D. 1984, *Nature*, 310, 557

# Danksagung

An dieser Stelle möchte ich mich bei allen Personen bedanken, die mich bei der Erstellung dieser Arbeit unterstützt haben. Vielen Dank an

- Prof. Dr. Christopher van Eldik für die Vergabe dieses interessanten Themas, für die vielen hilfreichen Diskussionen und Anregungen und die Betreuung dieser Masterarbeit.
- Prof. Dr. Jörn Wilms für die Übernahme des Zweitgutachtens.
- Dr. Daniil Nekrassov für die Bereitstellung der CS-map.
- die gesamte H.E.S.S. Gruppe in Erlangen. Für die nette Aufnahme in das Team und die Hilfsbereitschaft, auch vor allem am Anfang der Arbeit. Bei Steffi und Susanne besonders für die Hilfe und das Beantworten unzähliger Fragen in der Phase des Schreibens.
- Steffi für das Korrekturlesen meiner Arbeit und die vielen hilfreichen Anmerkungen.
- meine Zimmerkollegen Stefan und Andreas – für eine super Zeit, die wir in diesem Jahr gemeinsam hatten, dafür dass eigentlich immer gute Stimmung im Büro war, und dass es auch immer mal was zum Lachen gab. Vor allem aber auch vielen Dank für die Hilfsbereitschaft und dafür, dass immer Zeit war für die vielen Diskussionen, die wir geführt haben (wo ist der Statistiker... also: ein Mathematiker würde dazu sagen...).
- Sebastian Eibl für den ein oder anderen guten Ratschlag und die gegenseitige Unterstützung während unseres gemeinsamen Studiums.
- meine Familie (vor allem meine Eltern) ohne deren Unterstützung weder das Studium noch die Masterarbeit in dieser Form möglich gewesen wäre.
- meine Freundin Julia für das Korrekturlesen meiner Arbeit und die Unterstützung während meines gesamten Studiums – danke!



# Erklärung

Ich bestätige hiermit, dass ich die vorliegende Masterarbeit selbständig verfasst und keine anderen als die angegebenen Quellen und Hilfsmittel verwendet habe.

Erlangen, den 28. Oktober 2014